

RESEARCH ARTICLE

10.1029/2018EA000375

Special Section:

Science and Exploration of the Moon, Near-Earth Asteroids, and the Moons of Mars

This article is a companion to Young et al. (2018), <https://doi.org/10.1029/2018EA000378>.

Key Points:

- Infrared spectral imaging can capture valuable geological information unattainable by other methods
- Ground-based imaging provides a critical link in scale between orbital measurements and individual sampling sites
- Advantages of infrared spectral imaging may benefit future planetary surface missions

Correspondence to:

G. Ito,
gen.ito@stonybrook.edu;
gen.ito@nasa.gov

Citation:

Ito, G., Rogers, A. D., Young, K. E., Bleacher, J. E., Edwards, C. S., Hinrichs, J., et al. (2018). Incorporation of portable infrared spectral imaging into planetary geological field work: Analog studies at Kilauea Volcano, Hawaii, and Potrillo Volcanic Field, New Mexico. *Earth and Space Science*, 5, 676–696. <https://doi.org/10.1029/2018EA000375>

Received 9 FEB 2018

Accepted 30 MAY 2018

Accepted article online 27 SEP 2018

Published online 5 NOV 2018

Incorporation of Portable Infrared Spectral Imaging Into Planetary Geological Field Work: Analog Studies at Kilauea Volcano, Hawaii, and Potrillo Volcanic Field, New Mexico

Gen Ito^{1,2} , A. Deanne Rogers¹ , Kelsey E. Young³ , Jacob E. Bleacher⁴, Christopher S. Edwards⁵ , John Hinrichs⁶, Casey I. Honniball^{7,8}, Paul G. Lucey^{6,7,8}, Daniel Piquero⁶, Byron Wolfe⁶, and Timothy D. Glotch¹ 

¹Department of Geosciences, Stony Brook University, Stony Brook, NY, USA, ²Now at NASA Goddard Institute for Space Studies, New York, NY, USA, ³El Paso/Jacobs JETS Contract at NASA Johnson Space Center, University of Texas, Houston, TX, USA, ⁴NASA Goddard Space Flight Center, Greenbelt, MD, USA, ⁵Department of Physics and Astronomy, Northern Arizona University, Flagstaff, AZ, USA, ⁶Spectrum Photonics, Inc., Honolulu, HI, USA, ⁷Hawaii Institute of Geophysics and Planetology, University of Hawai'i at Mānoa, Honolulu, HI, USA, ⁸Department of Geology and Geophysics, University of Hawai'i at Mānoa, Honolulu, HI, USA

Abstract During geological work for future planetary missions, portable/hand-held infrared spectral imaging instruments have the potential to significantly benefit science objectives. We assess how ground-based infrared spectral imaging can be incorporated into geological field work in a planetary setting through a series of field campaigns at two analog sites: Kilauea Volcano, Hawaii, and Potrillo Volcanic Field, New Mexico. For this study, we utilize thermal infrared emission spectroscopy (8–13 μm) because this wavelength range is sensitive to major silicate spectral features and covers the terrestrial atmospheric window; however, our conclusions are applicable to other forms of infrared imaging (e.g., near-infrared reflectance spectroscopy). We demonstrate the ways in which spectral imaging could potentially enhance the science return and/or efficiency of traditional geological field work. Benefits include the following: documentation of major compositional variations within scenes, the ability to detect visually subtle and/or concealed variability in (sub) units, and the ability to characterize remote and/or inaccessible outcrops. These advantages could help field workers rapidly document sample context and develop strategic work plans. Furthermore, ground-based imaging provides a critical link between orbital/aerial imaging scales and sampling scales. Last, infrared spectral imaging data may be combined with in situ measurement techniques, such as X-ray fluorescence, as well as other ground-based remote sensing techniques, such as LIDAR (Light Detection And Ranging), to maximize geological understanding of the work area.

Plain Language Summary Future missions to planetary objects are expected to have increasingly more human and rover components in surface exploration. To aid the explorers in conducting scientific tasks, portable instruments will likely be invaluable. Currently, knowledge of instrument suitability and most effective incorporation strategies are not sufficiently developed. As one of the first steps in this development process, we assess the fundamental capabilities of portable imaging technique in providing critical information for geological field work on planetary surfaces. Portable imaging, operating in the thermal infrared (8–13 μm), captured crucial data regarding rock/mineral types at field sites analogous to planetary settings. Value brought forth by portable infrared imaging is substantial, and this technique has the potential to benefit effective geological field work, which may lead to maximizing scientific return from missions. This finding and accompanying analyses presented here serve as a foundation for further development of instruments and mission strategies.

1. Introduction

Hardware and operation tests conducted in field campaigns that simulate planetary scenarios frequently bring valuable knowledge that contributes to preparation for human missions to planetary bodies (e.g., Desert Research and Technology Studies; Abercromby et al., 2013; Eppler et al., 2013; Hörz et al., 2013; Hurtado et al., 2013; Ross et al., 2013; Young et al., 2013). The sample collection workflow during future human missions to planetary bodies will likely benefit from portable/hand-held geochemical and

©2018. The Authors.

This is an open access article under the terms of the Creative Commons Attribution-NonCommercial-NoDerivs License, which permits use and distribution in any medium, provided the original work is properly cited, the use is non-commercial and no modifications or adaptations are made.

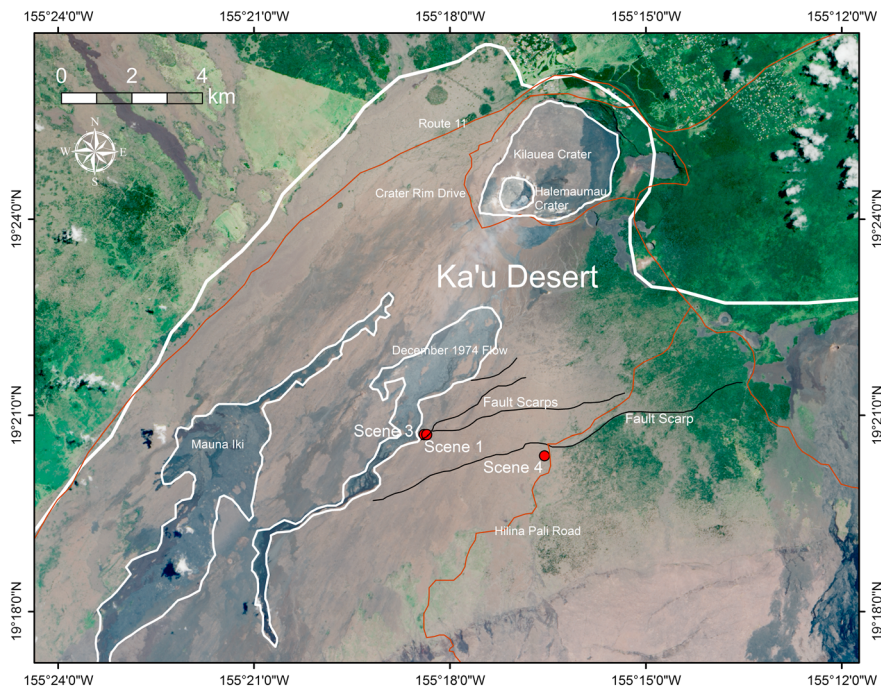


Figure 1. Map of the field site, Kilauea Volcano, Hawaii. Imaging and sampling locations referred in the text are labeled with red points and summarized in Table 1. Landsat 8 satellite imagery is used.

mineralogical instruments (Hurtado et al., 2013; Young et al., 2013, 2016, 2018). Rapid, in situ analyses of geological materials will allow astronauts to make strategic and tactical decisions most fit for the scientific objectives of the mission. Thus, crewmembers can quickly proceed to sample collection and work with the science team to develop and later test new hypotheses. Furthermore, ground- or rover-based spectral imagers allow for rapid compositional documentation of the site and sample context.

As part of the Remote, In Situ, and Synchrotron Studies for Science and Exploration (RIS⁴E) node of NASA's Solar System Exploration Research Virtual Institute effort (Glotch et al., 2015), we assess the incorporation of infrared spectral imaging into geological field work through expeditions designed to test the utility of such measurements at terrestrial analog sites. We aim to assess the broad-scale concept of using infrared spectral imaging in geological field work, making the assessments applicable to different wavelengths, such as, but not limited to, the thermal (5–50 μ m) and visible/near-infrared (VNIR) (0.4–4 μ m) ranges. One of the primary objectives is to understand the degree to which instruments, which can have significant operational overhead, can enhance the science return of a planetary field mission. This work presents the outcomes and assessments of the incorporation efforts of portable infrared spectral imaging during our expeditions at the RIS⁴E field sites, Kilauea Volcano, Hawaii, and Potrillo Volcanic Field, New Mexico. A second article in this volume summarizes the lessons learned from the full instrumentation suite tested at both RIS⁴E sites (Young et al., 2018).

2. Study Sites

2.1. Kilauea Volcano, Hawaii

A volcanic lava field was chosen as our primary field site because the landscape and mineralogy represent a reasonable analog to surfaces of the Moon, Mars, and some differentiated asteroids. Our field expeditions took place at and near the December 1974 Flow of Kilauea Volcano, Hawaii (Figure 1). The variety of volcanic landforms and materials found here, including but not limited to lava flows, ash deposits, fumaroles, and pit craters (Easton, 1987), makes this area well suited for analog studies.

The field site lies within the Ka'u Desert, a semiarid region to the southwest of Kilauea caldera with very limited amounts of vegetation (Figure 1). The Ka'u Desert is characterized by basalt flows, tephra, and deposits of reworked tephra debris (Malin et al., 1983). The basalt flows in this area are part of the Puna Basalt group, in

Table 1
GPS Coordinates of Field Scenes

Scene no.	Field site	Latitude	Longitude
1	Kilauea	19°20'41.9316"N	155°18'21.7908"W
2	Potrillo	31°57'31.0926"N	106°58'07.0170"W
3	Kilauea	19°20'42.3708"N	155°18'23.7888"W
4	Kilauea	19°20'22.4592"N	155°16'33.4452"W
5	Potrillo	31°57'25.3008"N	106°57'22.4316"W

Note. Scene numbers correspond to the field site maps (Figures 1, 2, and 16) and the scenes presented in the results (Figures 5, 8, 10, 12, and 15).

which Kipka Nene flows (1,000–1,500 years B.P.), Kalue flows (500–750 years B.P.), Observatory flows (250–350 years B.P.), and the December 1974 Flow (Holcomb, 1987) are encountered in our work. The tephra, known as the Keanakāko'i Formation, is derived from periodic eruptions, including the 1790 eruption that is believed to compose a large portion of the formation and consists of ash, lapilli (pisolites), pumice, and blocks of accessory materials (Easton, 1987; Malin et al., 1983). The Keanakāko'i Formation exposed on the surface is typically the *scabby* upper lithic unit that has a case-hardened crust of sand-to-silt-sized particles (Malin et al., 1983). Fragments from the basalt flows and lithic unit accumulate in gravelly, dune-like *lag gravel terrains* (Malin et al., 1983;

Tirsch et al., 2012). Basalt flows, Keanakāko'i tephra, and the lag gravel terrain are often the three major features captured in spectral imaging. The lag gravel terrain may contain sand- to gravel-sized clasts.

Mineralogically, this volcanic field is characterized by glassy basalts containing olivine, pyroxene, and plagioclase phenocrysts (Wright, 1971) and eolian sediment deposits dominated by olivine, pyroxene, plagioclase, and glasses (Tirsch et al., 2012). The surfaces of lava flows often exhibit evidence of weathering and alteration, seen as thin coatings formed by leaching precipitation and dissolution precipitation (e.g., Minitti et al., 2007). Because the mineralogy and spectral properties of geologic materials found here are already reasonably well characterized (e.g., Abbot et al., 2013; Abrams et al., 1991; Chemtob et al., 2010; Crisp et al., 1990; Kahle et al., 1988; Minitti et al., 2007; Schiffman et al., 2006; Seelos et al., 2010; Tirsch et al., 2012), the December 1974 Flow area at Kilauea Volcano is a well-suited field site for testing spectral imaging and sample collection procedures.

2.2. Potrillo Volcanic Field, New Mexico

Located in south central New Mexico, the Potrillo Volcanic Field lies in the region known as the southern Rio Grande rift. The Rio Grande rift was partly created by Tertiary tectonic extension, which led to active magmatism in the Quaternary (<80 ka) that established much of the volcanic features observable at Potrillo today (Thompson et al., 2005). Some of the notable volcanic features include cinder cones, shield volcanoes, lava flows, and maar craters (Anthony et al., 1992). Like Kilauea, this volcanic field was created by basaltic magmatism, and compositional and physical properties of the geologic materials encountered here are relevant to those on the Moon, Mars, and some differentiated asteroids. However, one difference between the two volcanic fields is that the basalt composition at Potrillo is alkalic, as opposed to tholeiitic at Kilauea.

Among the many volcanic features found at Potrillo Volcanic Field, the maar crater named Kilbourne Hole (Figure 2) is of particular interest for spectral imaging. A maar crater is a large steep-sided depression in the ground produced by an explosion that can remove extensive volumes of surface and subsurface rocks. The cause of maar explosions is the pressure built by evaporating groundwater that came in close proximity to the rising magma. The volcanic eruption involving magma and evaporating water, known as phreatomagmatic eruption, formed rhyolitic ashfall tuffs and pyroclastic surge deposits with ejecta such as lapilli and bombs on the rims of maar craters (Darton, 1916; Seager, 1987). The explosion and removal of upper rocks allow deeper materials to ascend and become exposed on the new surface. Because of this, mantle xenoliths are scattered around Kilbourne Hole and embedded in the wall rocks. This presents a unique setting, especially compared to basalt-dominated Kilauea, for spectral imaging to capture important variabilities within field scenes.

3. Methodology

Ground-based infrared spectral imaging can be carried out in various portions of the electromagnetic energy spectrum, including the visible/near-infrared wavelength range (solar reflectance spectroscopy; e.g., Greenberger, Mustard, Cloutis, Mann, et al., 2015; Greenberger, Mustard, Ehlmann, et al., 2015; Greenberger, Mustard, Cloutis, Pratt, et al., 2015) and the thermal infrared range (thermal emission spectroscopy; e.g., Christensen et al., 2003; Ramsey & Harris, 2012). Both techniques provide complementary mineralogical information, and either/both could potentially be used in future human missions to lunar, asteroid, and other planetary surfaces. In this work, the mineralogical characteristics of geological materials in the field site were inferred from thermal emission spectroscopy.



Figure 2. Map of the field site, Potrillo Volcanic Field, New Mexico. Kilbourne Hole and Hunt's Hole are maar craters. The West Potrillo Mountains are composed of hundreds of cinder cones. Imaging locations referred in the text are labeled with red points and summarized in Table 1. Landsat 8 satellite imagery is used.

3.1. Thermal Emission Spectroscopy

Vibrational motions present in crystal lattices of solids are related to their elemental composition and crystal structure (Farmer, 1974; Wilson et al., 1955). The fundamental vibrational frequencies of minerals, mineraloids, and glasses are typically in the thermal infrared wavelengths (~ 5 to $50 \mu\text{m}$). Variations in absorption features of thermal infrared spectra of geologic materials mirror variations in their composition and crystal structure, and this property can be used to determine mineral species and identify rock types (Lyon, 1963; Salisbury, 1993; Salisbury et al., 1991; Walter & Salisbury, 1989). The value of thermal emission spectroscopy in remote mineralogical and geological analyses has been shown through many studies in the past (Christensen et al., 2001, 2003, 2000; Christensen & Harrison, 1993; Cooper et al., 2012; Feely & Christensen, 1999; Hamilton et al., 2001; Hamilton & Christensen, 2000; Kahle et al., 1993; Lane & Christensen, 1997, 1998; Lyon, 1963; Rowan et al., 2003, 2005; Salisbury & Walter, 1989; Salisbury et al., 1991; Salisbury, 1993; Vincent & Thomson, 1972; Wyatt et al., 2001).

In this study, particularly at Kilauea, we frequently refer to the two major spectral features in the thermal infrared that are ubiquitously encountered: the broad feature in the ~ 800 to $\sim 1,200\text{-cm}^{-1}$ region that is



Figure 3. (left) Multispectral frame and (right) hyperspectral scanning imaging instruments used in this work.

characteristic of glassy basalts and the prominent, narrower spectral feature centered near $1,100\text{ cm}^{-1}$, attributed to opaline silica (e.g., Kahle et al., 1988; Minitti et al., 2007).

3.2. Instruments and Image Processing Overview

Spectral emissivity is derived from thermal infrared spectral radiance measurements. In this work, we used a scanning hyperspectral imager from Spectrum Photonics, Inc., of Honolulu, HI. The hyperspectral imager features 35 bands in the $8\text{--}13\text{-}\mu\text{m}$ wavelength range with a spectral resolution of 13.3 cm^{-1} . The instrument is optically identical to an instrument described in Gabrieli et al. (2016) and was repackaged for improved field portability by Spectrum Photonics (Figure 3). The instrument is operated as a panoramic push broom imager with a vertical field of view of 9° sampled by 1276×200 pixels. It uses a 320×256 microbolometer array (FLIR Photon) for infrared detection, and data are corrected for pixel to pixel nonuniformity using observations of internal blackbodies at two temperatures (Wright et al., 2013). Pixels near the edge of the frame are vignetted and trimmed for the final data set from 256 to 200 pixels. Further data calibration and reduction are also described in Gabrieli et al. (2016). This instrument was supplemented by our in-house assembled multispectral frame imager that has five bands in the $8\text{--}13\text{-}\mu\text{m}$ range, $25^\circ \times 19^\circ$ field of view, and 640×480 pixel detector (Figure 3). The wavelength range covered by both of these instruments corresponds to the range of highest terrestrial atmospheric transmittance in the thermal infrared and to the major characteristic spectral features of silicate minerals. The filter functions and artifact correction for the multispectral frame imager are described in the appendix (sections A1 and A5). Details of radiance calibration, atmospheric correction, and radiance-to-emissivity conversion are also provided in the appendix (sections A2–A4). We note that the aspects of the calibration require known targets; therefore, when the working conditions allowed, we placed calibration targets into the scenes (Scenes 2 and 4). Scene calibration targets would not be necessary for a planetary mission; however, this is described further in section A3.

In this work, field-based spectral emissivity measurements are displayed as false color images, using three wavelengths selected for red-green-blue composites. These red-green-blue images are enhanced with the decorrelation stretch (DCS) technique. The DCS technique transforms three bands of data to principal components and stretches the data values to more efficiently use the digital color scale (Gillespie et al., 1986; Sabine, 1999). This leads to increased color contrast and enhanced display of differences in emissivity or radiance spectra of materials captured in the images.

The magnitude of radiance (which depends on surface temperature, section A2) determines the quality of the interpretable information from emission spectroscopy. Large radiance values lead to higher signal-to-noise ratios, leading to more precise derivation of emissivity spectra and higher quality of processed infrared images. Generally, in the field, sunny, warm conditions yield large radiance values, and conversely, cloudy, cool conditions lead to low radiance values and poorer image quality. We conducted measurements in mostly sunny and very sunny conditions at Kilauea and Potrillo field sites, respectively. For a planetary mission that incorporates a thermal infrared imager, the minimum temperatures and acquisition times

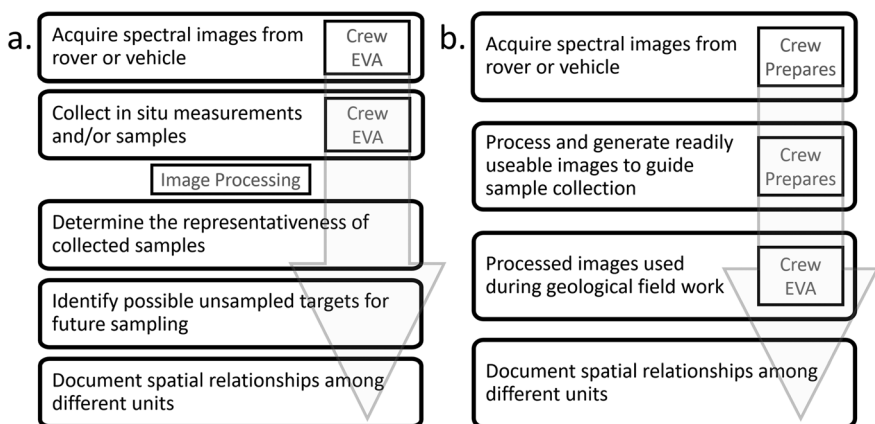


Figure 4. (a) Sampling workflow adopted in this study with limited technologies and resources of our current spectral instruments and data reduction algorithms. (b) A potential sample collection workflow during planetary geological field work, where infrared spectral imaging is used in the tactical decision-making process for sampling.

required to achieve adequate spectral information would depend on the instrument design; a detailed discussion of these factors is beyond the scope of this work.

3.3. Incorporation of Spectral Imaging Into Field Work

Spectral imaging is used as one of the aids to members of the RIS⁴E team that simulate geological field work during Extravehicular Activities (EVA) on other planetary surfaces (Young et al., 2018). The sampling workflow adopted in this work using our currently available spectral instruments is shown in Figure 4a. Spectral images are acquired during EVA, and then in situ chemical or mineralogical point measurements are acquired by the field team. In some locations, samples are also collected (Young et al., 2016, 2018). Images are processed later by the instrument team members and provided to the field team in order to determine the representation of collected samples and/or in situ measurements in a particular location, identify possible unsampled targets for future analysis, and document spatial relationships among different units. The workflow shown here is suited for our present study, though alternative workflows, such as spectral imaging used in tactical decision making for sampling, could also be considered (Figure 4b).

3.4. Laboratory Techniques

3.4.1. Infrared Emission Spectral Measurement

In order to validate the accuracy of our field-based, nondestructive spectral measurements, a few samples were collected from units of interest and measured in the laboratory. During sampling, care was taken to minimize the impact to the rock exposures (naturally broken pieces were selected) and the volume of sample collection. Samples were taken to Stony Brook University's Center for Planetary Exploration, and their infrared spectra were measured for comparison to spectra derived from imaging instruments. Emissivity (hemispherical) spectra were derived over the frequency range 400–1,600 cm⁻¹ (6.25–25 μm) using a Nicolet 6700 Fourier transform infrared spectrometer employing the methods of Ruff et al. (1997). This method is equivalent to the procedure of radiance measurement and its conversion to emissivity presented in section A2.

3.4.2. Particle Size Measurement

For particulate materials, increased scattering of light due to the presence of small particles (in relation to wavelength) has a consequential impact on emissivity spectra. Therefore, to better interpret our laboratory and field measurements of the Keanakāko'i tephra sands, particle size distributions were measured using a Malvern Mastersizer 2000 laser diffractometer available in the Department of Geosciences at Stony Brook University. Conventional laser diffractometry uses Mie theory (van de Hulst, 1957) to retrieve particle sizes from scattering patterns of laser light induced on particles suspended in water or other selected medium. We followed a technique from Sperazza et al. (2004) who documented a precision of ~5% at two standard deviations for fine particles (<10 μm) to obtain best results; however, any use of conventional laser diffractometry based on Mie theory must be accompanied with understandings of assumptions taken in its instrumentation, such as the use of volume equivalent spheres to represent particles (Mishchenko, 2009, 2014).

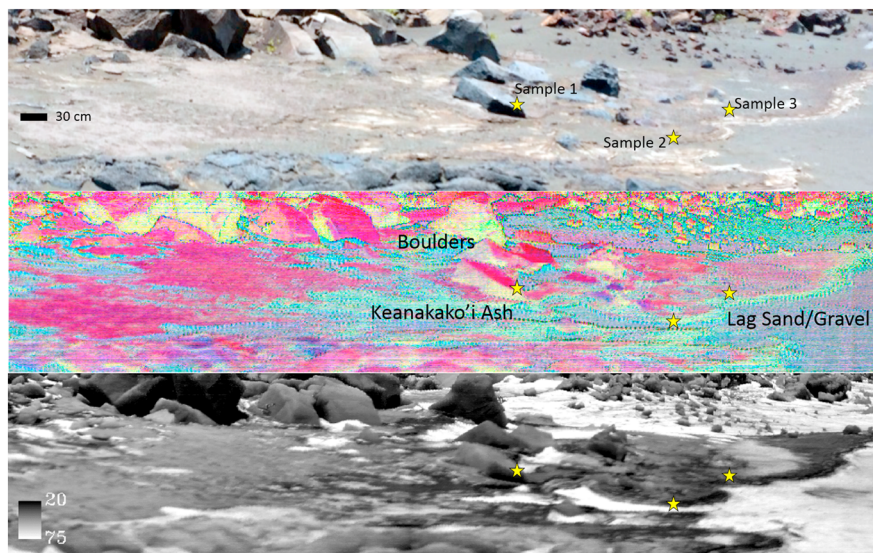


Figure 5. Scene 1, from the Kilauea field site, seen in visible light (top), false color infrared (middle) derived from thermal emissivity spectra, and temperature (bottom) in degrees Celsius. The spectral image is from hyperspectral imaging and has been decorrelation stretched where blue, green, and red were assigned to the wavelengths 8.5, 9.1, and 11.3 μm , respectively. Shadows and vertical rock faces appear yellow-green in this wavelength combination (sections 3.2 and 5). Sampling locations for laboratory analysis are indicated with stars.

4. Results

The goal of this work is to assess the advantages and potential limitations of infrared spectral imaging when used as part of a geological field campaign. In this section, we illustrate this by showing field scenes, both in visible (digital camera photographs) and infrared, and highlighting three potential benefits of spectral imaging that were noted in the process of the field team's sampling campaign. Results from both the hyperspectral and multispectral instruments are shown.

4.1. Documentation of Major Compositional Variations Within Scenes

In Scene 1 (Ka'ū desert, Hawaii), three major units of geological materials are defined, where red/magenta, cyan, and blue-purple areas in the false color image correspond to boulders/large rocks, ash (Keanakako'i Formation), and lag sand/gravel terrain, respectively (Figure 5). This unit distinction captured with spectral imaging is consistent with first-order observations made with the naked eye, serving as a rough confirmation that the compositional and/or textural variabilities can be detected with spectral imaging. The false color images enhance the ease in which geological variability can be recognized, however.

Spectra of the samples collected from this scene are compared with the corresponding locations within the spectral image (Figure 6). Spectra from pixels in the field hyperspectral image and from the laboratory measurements agree well, serving as another confirmation that our spectral imaging technique is accurate and capable of detecting and discriminating spectral signatures of the geological materials.

Both the narrow feature ($1,100 \text{ cm}^{-1}$) caused by opaline silica and the broad spectral feature (~ 800 to $\sim 1,200 \text{ cm}^{-1}$) of glassy basalt are present, with varying intensities, in the spectra of the three major units. The narrow band at $1,100 \text{ cm}^{-1}$ is the deepest for boulders and becomes less prominent for lag sand/gravels (Figure 6). This feature is minimally observable in Keanakāko'i ash (Figure 6). Opaline silica coating dominates the spectral signature of basaltic boulders and lag sand/gravel; the broad spectral feature of glassy basalt is largely obscured by the opaline silica band except for the ~ 800 to $\sim 900 \text{ cm}^{-1}$ range. Keanakāko'i ash mainly exhibits the broad absorption characteristic of glassy basalt, though with shallow band depth; a weak feature consistent with opaline silica is also observed in the field spectrum. The laboratory spectra of Keanakāko'i ash do not show as much indication of opaline silica possibly due to mixing of the surface and interior particles that cannot be avoided when collecting samples in a storage container for later laboratory measurement.

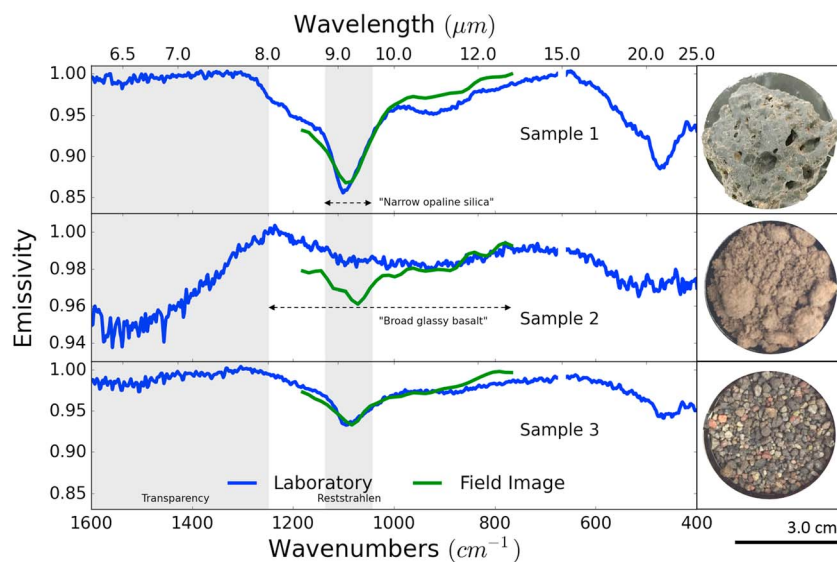


Figure 6. Comparison of emissivity spectra of laboratory samples with the corresponding locations on the field hyperspectral spectral image. Sample 1: boulder. Sample 2: Keanakāko'i ash. Sample 3: lag sand/gravel. Laboratory spectra around 670 cm^{-1} are masked due to absorption caused by CO_2 gas that could not be fully purged. A 3×3 pixel average is used for the field image spectra. Spectral features referred in the text are labeled *Transparency*, *Reststrahlen*, *Narrow opaline silica*, and *Broad glassy basalt*.

The shallow feature depth in the ~ 800 to $\sim 1,200\text{-cm}^{-1}$ region and low emissivity at higher frequencies of Keanakāko'i tephra sands could be due to the effect of small particle size (Figure 7). The spectral contrast of silicate reststrahlen features and transparency features at volume scattering high frequencies decrease and increase, respectively, in intensity as the size of materials decreases (Conel, 1969; Hunt & Vincent, 1968; Ito et al., 2017; Moersch & Christensen, 1995; Mustard & Hays, 1997; Pitman et al., 2005; Ruff et al., 2011; Salisbury, 1993). More detailed inferences regarding the ash could be obtained using light-scattering models (e.g., Ito et al., 2018). These compositional and textural variations are important for effective geological interpretation of surface materials and are captured by spectral imaging.

Scene 2 is from Kilbourne Hole of the Potrillo field site and dominated by sediments derived from the surrounding volcanic ash and sedimentary rocks (Figure 8). These sediments are indicated with red to purple color in the false color infrared image. Pebble- to cobble-sized xenoliths prominently appear as royal blue in the false color image. Emissivity spectra of these xenoliths were measured in the laboratory, and the xenoliths were confirmed to be predominantly olivine (Figure 9). As with Scene 1, spectral imaging detects major compositional variations within the scene.

4.2. Detection of Concealed Variability Within Units (Kīlauea)

Boulders and lag sand/gravel terrain are the major unit types found in Scene 3 (Figure 10). The lag sand/gravel unit shows spectral variability within itself, manifested as varying shades of blue and purple. By zooming in into the center of the image and applying the decorrelation stretch again only within the zoomed-in area, the variability within the lag sand/gravel unit can be better visualized. Within the zoomed-in area, two subtypes of the lag sand/gravel unit become more clearly apparent (Figure 10). The lower emissivity values from about $1,100$ to $1,180\text{ cm}^{-1}$ ($1,100\text{-cm}^{-1}$ feature) in the upper cyan region compared to the lower red/magenta region (Figures 10 and 11) could indicate that the lithic fragments and particles lack opaline silica coatings or could be attributed to a greater abundance of finer-grained ash. Though noticeable in spectral

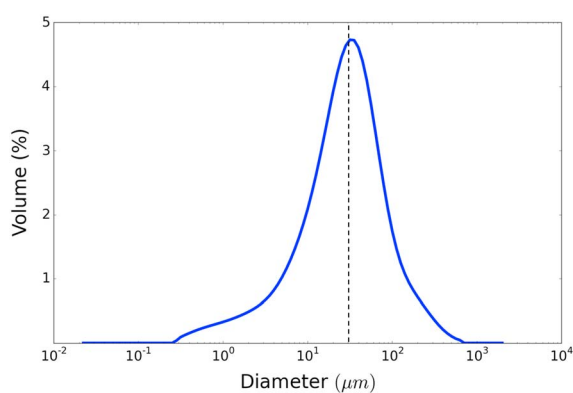


Figure 7. Particle size distribution of Keanakāko'i ash (sample 2 in Figure 6) measured using laser diffractometry. An approximate maximum particle diameter where scattering effects become considerable is indicated with the dashed line. A significant fraction of Keanakāko'i ash contains particles with diameters on the order of and smaller than the wavelengths used in spectral imaging ($8\text{--}13\text{ }\mu\text{m}$), which increases volume scattering and reduces spectral contrast of reststrahlen bands.

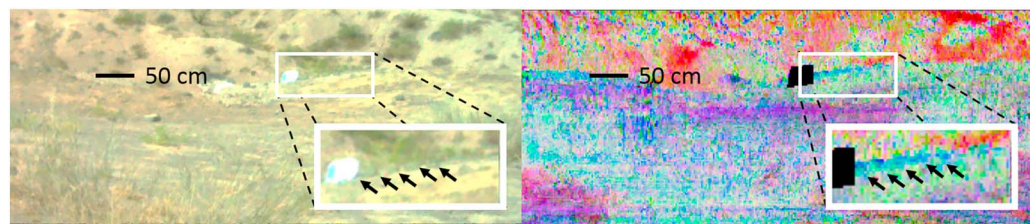


Figure 8. Scene 2, from the Potrillo field site, seen in visible light (left) and false color infrared (right) derived from thermal emissivity spectra. The spectral image is from hyperspectral imaging and has been decorrelation stretched where blue, green, and red were assigned to the wavelengths 8.5, 9.1, and 11.3 μm , respectively. Aluminum foil calibration target has been masked in the spectral image. The inserts magnify areas around xenoliths. Xenoliths, pointed by arrows in the inserts, were manually placed in a line near the foil panel to ensure that they would be captured in the field of view. Vegetation appears light blue-green.

images, using just the naked eye from some distance, this variability is visually subtle (Figure 10). This is an example where spectral imaging more effectively captures potentially important geological information than the naked eye.

Scene 4 includes an older flow, likely to be some components of Kalue (500–750 years B.P.) and/or Kipka Nene (1,000–1,500 years B.P.) flows (Holcomb, 1987), which lies in the vicinity of the December 1974 flow and is characterized by more weathered rocks and more abundant vegetation. This scene was acquired with multispectral imaging where the spectral resolution is coarser than that of hyperspectral imaging. Despite this limitation, variability within the scene is observed. As in the previous scenes, basalt flow, Keanakāko'i ash, and lag sand/gravel units are present. Similar to Scene 3, there are spectral variations in the lag sand/gravel terrain that manifest only as subtle color/textural variations in visible wavelengths. The lag sand/gravel unit that seems almost uniform in the visible image actually shows two subtypes in spectral imaging (Figure 12). The lower, light blue/purple colored portion of the lag sand/gravel unit has a deeper feature at $1,100 \text{ cm}^{-1}$ compared to the upper, dark red/blue colored portion (Figure 14). We confirmed the presence of this variability by returning to the site and conducting close-up color imaging of the region of interest (Figure 13), as

well as sampling each soil subtype for laboratory spectral analysis (Figure 14). We found that the upper section of the lag sand/gravel was richer in fine-grained Keanakāko'i ash and moss, leading to the lack of lower section's deep opal feature observed at $\sim 1,100 \text{ cm}^{-1}$.

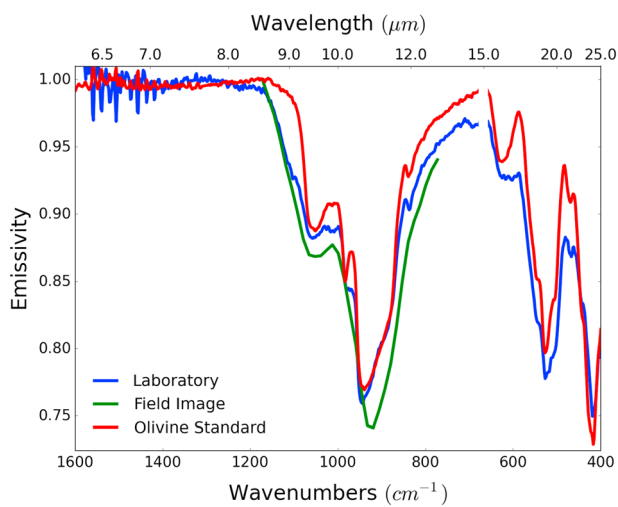


Figure 9. Thermal infrared emissivity spectrum of a xenolith sample from Scene 2 measured in the field with hyperspectral imaging and in the laboratory. Spectrum around 670 cm^{-1} is masked due to absorption caused by CO_2 gas that could not be fully purged. The field hyperspectral image spectrum has been corrected for downwelling radiance similar to the methods of Horton et al. (1998) but based on measured aluminum spectral emissivity (see also section A2). Six-pixel average is used for the field hyperspectral image spectrum. The olivine standard was taken from Christensen et al. (2000).

4.3. Characterization of Remote or Inaccessible Locations (Potrillo)

Scene 5 includes an outcrop of strata exposed on the southeastern wall of Kilbourne Hole (Figure 2). This outcrop was not accessible by the field team, and therefore, information captured remotely by spectral imaging was one of the limited and valuable resources to analyze this location. The major contact between the darker overlying rock unit and lighter underlying rock unit can be seen in both the visible and spectral images (Figures 15a–15c). Additional spectral variability, such as variations within the darker overlying and lighter underlying units, is also observed. To estimate the composition of these inaccessible units, spectra were averaged and extracted from regions of interest, based on color in the DCS image. Next, we modeled the spectra with a set of 19 laboratory spectra using a nonnegative linear least squares minimization routine (Lawson & Hanson, 1974; Rogers & Aharonson, 2008). For thermal emission spectra of rocks and coarse particulates ($>\sim 60 \mu\text{m}$), and using a library that captures the range of minerals present in the mixture, this technique is capable of retrieving areal mineral abundances to within 15% absolute accuracy (Feely & Christensen, 1999; Hamilton & Christensen, 2000; Ramsey & Christensen, 1998; Thorpe et al., 2015). Mineral detection limits depend on the mixture but generally range between ~ 5 and 15%

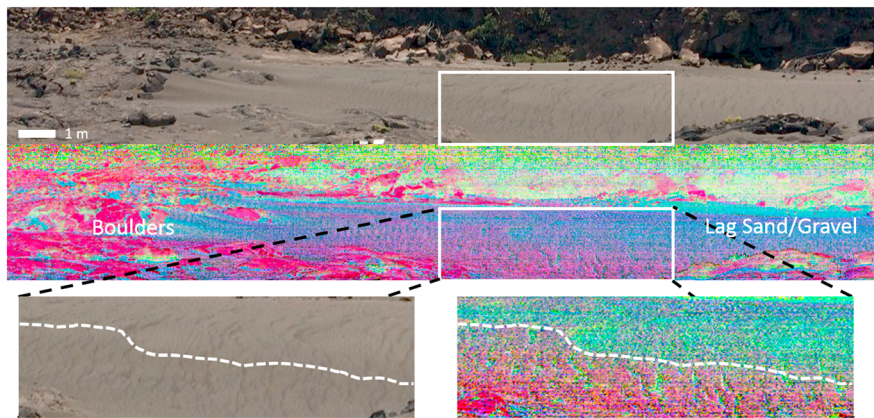


Figure 10. Scene 3, from the Kilauea field site, seen in visible light (top) and in false color infrared (middle) derived from thermal emissivity spectra. The spectral image is from hyperspectral imaging and has been decorrelation stretched where blue, green, and red were assigned to the wavelengths 8.5, 9.1, and 11.3 μm , respectively. Shadows, vertical rock faces, and vegetation appear yellow-green. A section of the lag sand/gravel unit that corresponds to the white boxes is zoomed in (bottom). Dashed line indicates an approximate division that highlights the variability within the lag sand/gravel unit.

(Christensen et al., 2000). The set of lab spectra was designed to incorporate known and/or likely minerals/rock types that would be present in the scene and included rhyolitic and basaltic rocks, two carbonate minerals, eight kaolinite and smectite minerals, an iron oxide (goethite), and olivine. Though additional iron oxides might be present in the scene, only goethite has spectral features within the wavelength range covered by the hyperspectral imager.

Figure 15d shows the model fits and derived mineral/rock abundances for the regions of interest. Variations in both rock type and alteration minerals are observed. For remote but accessible areas, images such as these could be acquired in scouting excursions to help in decision making for planning future traverses. In addition, there are scenarios in which collected samples could be related to distant/inaccessible outcrops through spectral imaging. For example, materials shed from outcrops upslope could be sampled and then related to intact stratigraphy imaged at distance.

5. Discussion

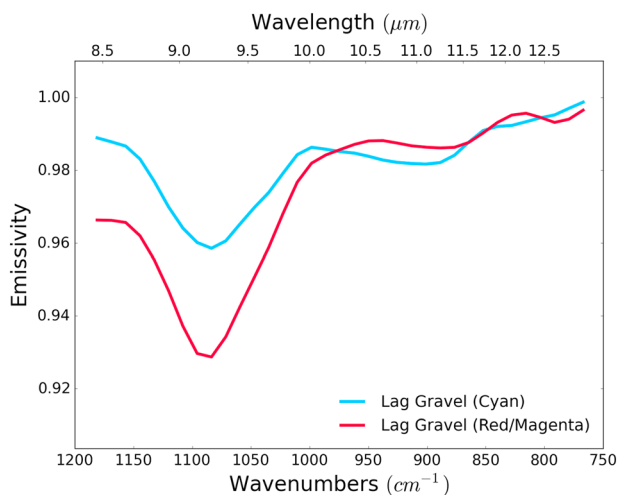


Figure 11. Representative spectra (field hyperspectral image) of cyan and red/magenta subtypes of lag sand/gravel terrain presented in the zoom-in image of Figure 10. A 10×5 pixel average was used.

We highlighted three major advantages in using infrared spectral imaging for geological field work: (1) documentation of major compositional variations, (2) enhancement of visibly subtle or concealed variability in (sub) units, and (3) characterization of inaccessible outcrops. The ability to document major compositional variations is important for understanding the geological context of the field site. The ability to detect visibly subtle or concealed variability substantially enhances the available knowledge about the field site, thus increasing the opportunity for discovery and advancing scientific insight. For inaccessible outcrops, hyperspectral imaging could provide compositional information where in situ measurements and/or sampling are not possible and could also be used to relate more accessible samples (such as displaced rocks) to intact stratigraphy. We envision that field workers will benefit by exploiting these advantages while conducting geological field work.

Another important aspect of ground-based spectral imaging is that it provides a critical link in scale between orbital infrared imaging and individual samples/in situ measurements. Spectral properties of the December 1974 Flow area of the Kilauea field site at a regional scale can be seen with false color infrared image of emissivity derived from the Thermal Infrared

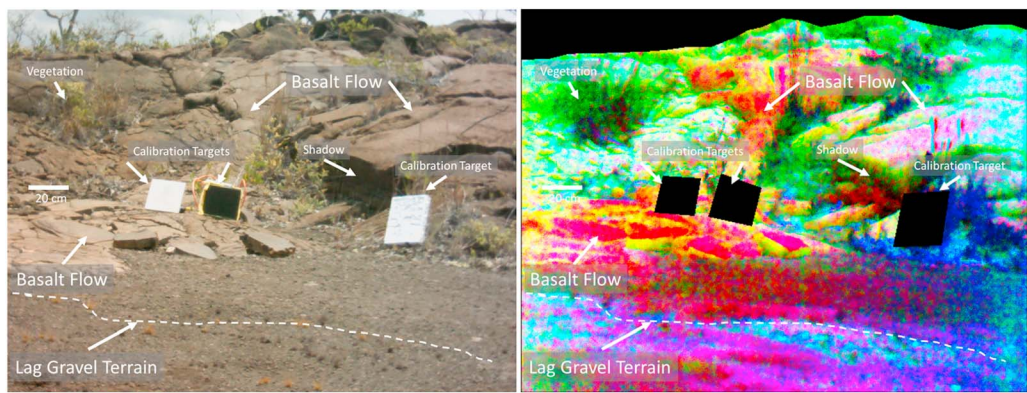


Figure 12. Scene 4, from the Kilauea field site, seen in visible light (left) and in false color infrared (right) derived from thermal emissivity spectra. The spectral image is from multispectral imaging and has been decorrelation stretched where blue, green, and red were assigned to 8.6-, 9.1-, and 11.3- μm wavelengths, respectively. Dashed line indicates an approximate division that highlights the variability within the lag sand/gravel unit. Infrared image has been enhanced with histogram stretching, and calibration targets and the sky have been masked prior to decorrelation stretch.

Multispectral Scanner (TIMS; Kahle & Goetz, 1983), which is an airborne instrument that has flown over Kilauea (Figure 16). The TIMS image was processed using the DCS technique, with similar wavelength combinations to those used for the ground-based field scenes. As in Scenes 1, 3, and 4, red/magenta, green, and cyan regions correspond to high abundances of glassy basalts, shadowed or soil-like (particulate) surfaces, and lag sand/gravel terrains, respectively. The TIMS image indicates that Scenes 1, 3, and their vicinity are mostly light green, suggesting a soil-like surface, but as seen in ground-based images, there are substantial variabilities in material types found at these scenes. Variabilities observed in ground-based imaging are too fine to be captured with aerial or orbital imaging. Ground-based spectral images act as a connection between these regional- or global-scale maps and individual samples, and they play a part in providing critical contextual information of the collected samples and/or in situ measurements.

The workflow adopted in this work (Figure 4a) is based on limited technology and currently available commercial resources. The time needed to make measurements in the field ranges from approximately 15 to 35 min; this time includes tripod and calibration target setup (Young et al., 2018). Furthermore, emissivity derivation and false colored image production requires an access to a computer and necessitates more time. However, data acquisition and production time is expected to decrease substantially for an instrument and data processing pipeline that have been streamlined for the target body and mission objectives. Advanced hardware and software could enable alternative workflows such as that shown in Figure 4b. Rapid data processing and reduction to simple compositional data products could allow images to be used in sampling/measurement decision making. For example, scans from a rover or a vehicle could be automated and completed while the astronauts prepare (e.g., space suits and other instruments) for EVA. Processed spectral images could then be available for use during geological field work. Spectral images could help to reduce sampling redundancy and/or deficiency in a seemingly uniform terrain. Furthermore, spectral images could be used to design a time-efficient path for collecting sample or in situ measurements.

Some measurement complexities cannot be solved with engineering or software development but instead must be solved with attention to Sun angle/time of day. For example, cold vertical rock faces within a few centimeters of the ground are affected by sidewelling radiance from warmer ash, sand, gravel, and other particulate surfaces that exhibit close to isotropic scattering. The combination of reflected light from nearby surfaces results in reduced spectral contrast (Figure 17). This effect is magnified for shadowed near-ground rock surfaces, which are even colder; their surface radiance contribution is minimized compared to that of reflected environmental radiance, and the resulting spectra are not diagnostic of

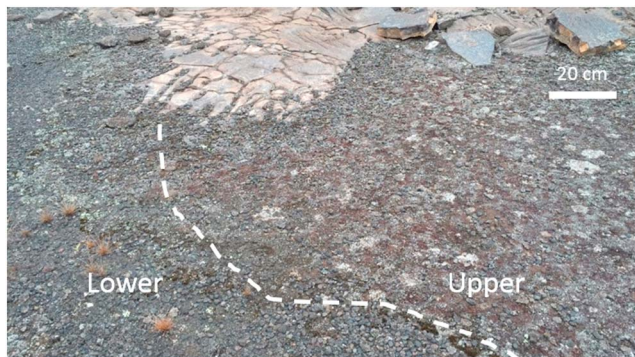


Figure 13. Digital camera photograph of the close reobservation of the lag sand/gravel unit in Scene 4. The approximate boundary between the two subtypes of lag sand/gravel is indicated with dashed lines.

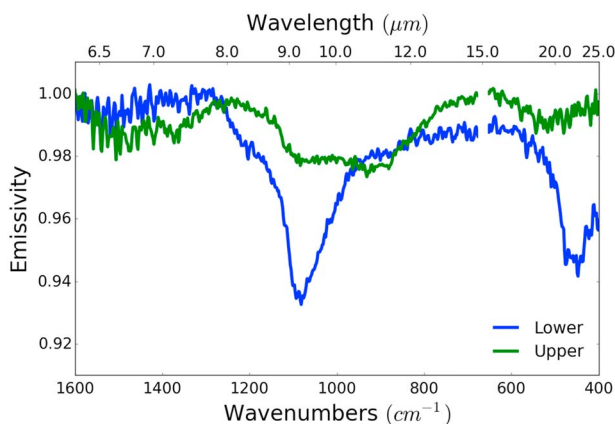


Figure 14. Spectral difference observed in laboratory samples of the two subtypes seen in the lag sand/gravel unit of Scene 4. Spectra around 670 cm^{-1} are masked due to absorption by CO_2 gas that could not be fully purged.

$1,100\text{ cm}^{-1}$ does not change substantially, until possibly 70° (Almeida, 1992; Ruff et al., 2011; Squyres et al., 2008). This effect was not observed in our study because the spectral imaging instruments do not adequately

the material (Figure 17). A more robust analysis of shadowed surfaces, with attention to distance from other surfaces and surface temperature, is needed to determine the conditions under which spectral analyses from such surfaces could still be used. Shadowed vertical rock faces are avoidable if the exposed surface is facing the light source; hence, time of day should be a consideration that is factored into ground-based imaging. Shadowed areas could be masked prior to the decorrelation stretch scheme in order to enhance the visual contrast of spectral variabilities within the scenes; however, care must be taken not to mask a disproportionate amount in order to preserve the spatial recognition provided by the images that is critically valuable for geological field work. A thorough investigation beyond the scope of this work is likely needed to find the proper balance for masking; thus, we have only masked geologically irrelevant objects (i.e., calibration targets and sky). Last, emissivity spectra from materials are affected by observation (emission) angle. For example, for opaline silica, the spectral band at $1,250\text{ cm}^{-1}$ is known to increase in band depth as the observation angle is increased, but the band at

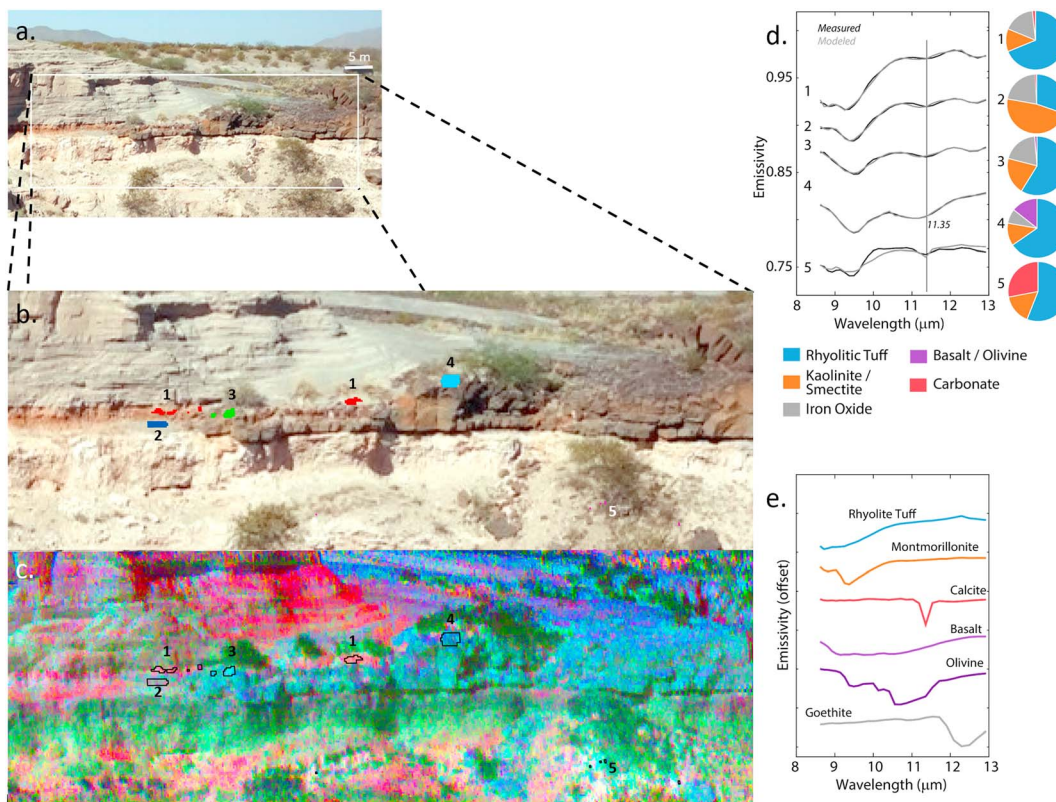


Figure 15. Scene 5, from the Potrillo field site. (a) Outcrop found on the southeastern wall of Kilbourne Hole. The zoom-in image is the scene of imaging (b) in visible and (c) in false color infrared derived from radiance spectra. The spectral image is from hyperspectral imaging and has been decorrelation stretched where blue, green, and red were assigned to the wavelengths 8.5 , 9.1 , and $11.3\text{ }\mu\text{m}$, respectively. Vegetation appears green. (d) Modeled emissivity spectra and mineral/rock abundances from regions of interest shown in (b and c). Poor model fit for Region 5 is likely due to either fine-grained particle sizes and/or a missing end-member from the spectral library used for fitting. Note that spectral feature at $11.35\text{ }\mu\text{m}$ is stronger in this spectrum compared to the others; this feature is consistent with calcium carbonate. (e) Representative selection of library spectra discussed in the text.

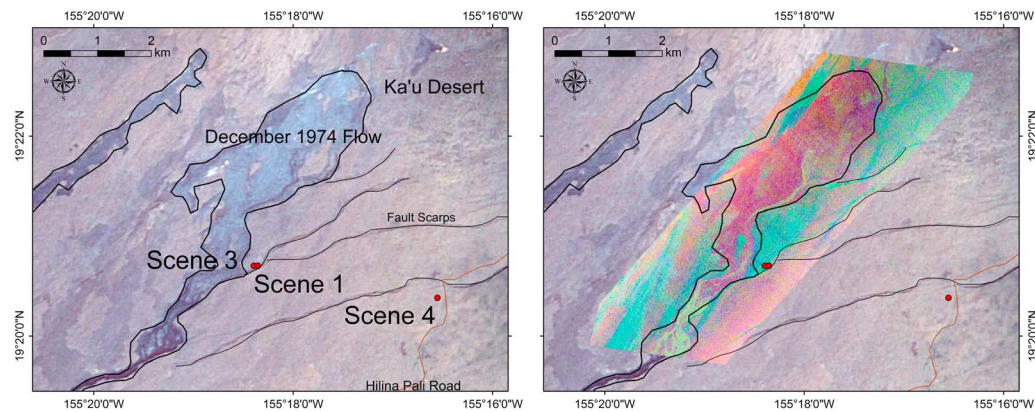


Figure 16. (left) The December 1974 Flow area of the Kilauea field site in satellite view and (right) the same area with an overlay of false color infrared aerial image from Thermal Infrared Multispectral Scanner (TIMS). Wavelengths used in the decorrelation stretch of the TIMS image are 8.5, 9.1, and 11.3 μm for blue, green, and red, respectively. Spatial resolution of TIMS image is approximately 2 m per pixel.

cover the $1,250\text{-cm}^{-1}$ feature; regardless, emission angle effects would need to be taken into account if spectral imaging is to be used for compositional interpretations. Such effects would not be important for detecting or documenting spectral variability, however. Although not investigated here, VNIR reflectance measurements would likely face similar issues with regard to shadows and observation angles.

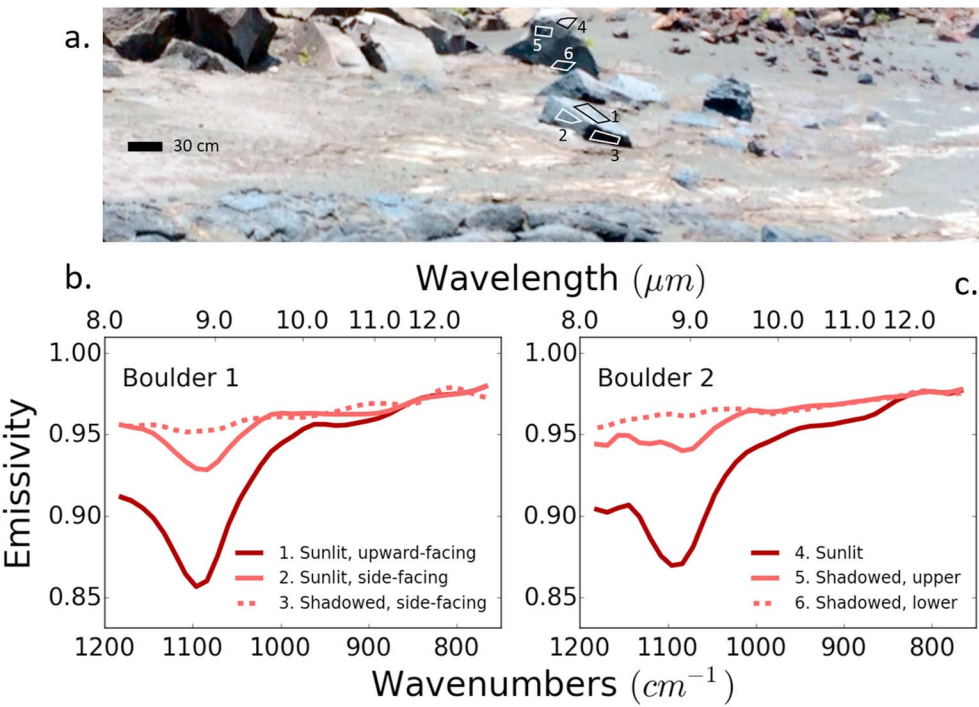


Figure 17. Examples of the effects of shadows and sidewelling radiance on the emissivity spectra from surfaces of interest. (a) Portion of scene 1 at the Kilauea field site. (b) Spectra from two sunlit faces and one shadowed face of boulder 1 (spots 1–3) are shown. The vertically oriented sunlit face is within 30 cm of the ground and exhibits slightly shallowed spectral features relative to the upward facing surface. The vertically oriented shadowed face exhibits greatly shallowed features. We preliminarily attribute the spectral shallowing to varying contributions of sidewelling radiance from nearby soils and rocks; however, it is possible that the vertically oriented faces of the boulder exhibit real spectral differences (e.g., thinner silica coating) than the upward facing surface of the boulder. Future work should investigate these issues in more detail. (c) From boulder 2 (spots 4–6), spectra from the sunlit face, and two spots on the shadowed face are shown. The shadowed spot closest to the ground shows the greatest amount of spectral shallowing.

6. Conclusions

We tested the concept of using portable infrared spectral imaging that could potentially benefit geological field work during future human missions to planetary bodies. Kilauea Volcano, Hawaii, and Potrillo Volcanic Field, New Mexico, were selected as our field sites due to their compositional and morphological similarities to the Moon, Mars, and some differentiated asteroids. At this stage, we used commercially available thermal imaging instruments.

The advantage of using infrared spectral imaging in geological field work is that, first, general variability within scenes of interest are detected. This was demonstrated in Scenes 1 and 2. Second, as shown in Scenes 3 and 4, spectral imaging has the capability to sense subtle variability that is difficult to capture with the naked eye and further present this potentially important information in a more recognizable way for the field workers. Third is the advantage of infrared spectral imaging as a remote sensing technique. Scene 5 displayed this advantage by characterizing geological variability of an outcrop inaccessible by field workers.

We discussed our visions and scenarios in which field workers may benefit by capitalizing on the advantages of infrared spectral imaging. This may manifest in making strategic work procedures or documentation of sample geological context. Furthermore, combining infrared spectral imaging data with data from other techniques, such as X-ray fluorescence spot data, LIDAR imagery, and aerial or orbital infrared images, will likely lead to maximizing geological understanding of the work area (Young et al., 2018). The advantages discussed here must be understood in the context of the limitations of our current instrumentation and the capability of thermal infrared spectroscopy itself used in natural settings.

We conclude that infrared spectral imaging is capable of detecting important geological information at terrestrial analog sites and is helpful for field team simulating EVA; therefore, infrared spectral imaging is a potentially useful tool for future planetary geological exploration. This fundamental assessment of infrared spectral imaging will be valuable to the engineering of future instruments specifically designing for missions and the development of planetary surface exploration methodologies.

Appendix A

A1. In-House Assembled Multispectral Imager

We customized a commercial FLIR (Forward Looking Infrared) T-640 Thermal Imager into a spectral instrument by mounting narrowband filters in front of the lens. The modification concept of commercially available products to fit our needs is similar to that presented by Prata and Bernardo (2009, 2014). Custom spectral filters were produced by Andover Corporation according to our specifications to transmit at 8.3, 8.6, 9.1, 10.3, and 11.3 μm (wave number 1,211.8, 1,163.2, 1,103.1, 971.7, and 883.3 cm^{-1} ; Figure A1).

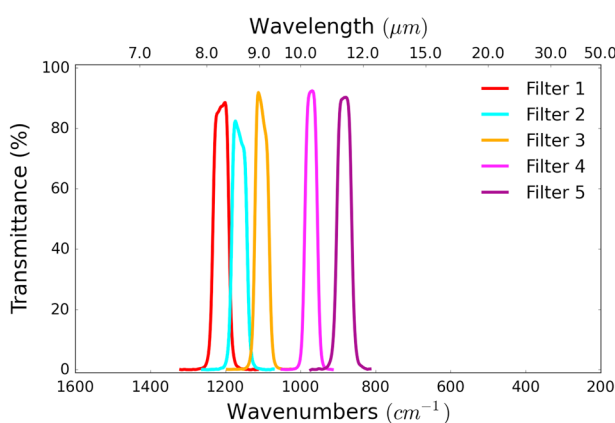


Figure A1. Wavelength-dependent transmittance of each of the five filters. Wavelength of peak transmittance are 8.3, 8.6, 9.1, 10.3, and 11.3 μm (wave number 1,211.8, 1,163.2, 1,103.1, 971.7, and 883.3 cm^{-1}) for filters 1, 2, 3, 4, and 5, respectively. Signals detected by the instrument using the filters are convolved to these filter functions.

A2. Radiance Calibration and Reduction to Emissivity

Spectral analysis in this study is based on emissivity spectra in the thermal infrared wavelengths. To derive emissivity, we equate radiances where the radiance measured by the detector ($L_{\text{meas}}(\lambda)$) is the sum of radiance emitted by targets in the scene ($L_{\text{targ et}}(\lambda)$), atmospheric downwelling radiance reflected by the objects ($L_{\text{atmDW}}(\lambda)$), radiance emitted by the atmosphere between the targets and the detector ($L_{\text{atm}}(\lambda)$), and reflected sidewelling radiance from adjacent surfaces ($L_{\text{sw}}(\lambda)$; Figure A2), leading to

$$L_{\text{meas}}(\lambda) = \tau_p(\lambda)(L_{\text{targ et}}(\lambda) + L_{\text{atmDW}}(\lambda) + L_{\text{sw}}(\lambda)) + L_{\text{atm}}(\lambda) \quad (\text{A1})$$

where each radiance term is dependent on wavelength (λ). Atmospheric transmissivity ($\tau_p(\lambda)$) is negligible (i.e., close to unity) in the 8–14- μm range, and thus, we ignore this term (Horton et al., 1998). The surface radiance $L_{\text{targ et}}(\lambda) = \varepsilon(\lambda)B(\lambda, T)$ is dependent on emissivity ($\varepsilon(\lambda)$) and the Planck blackbody function,

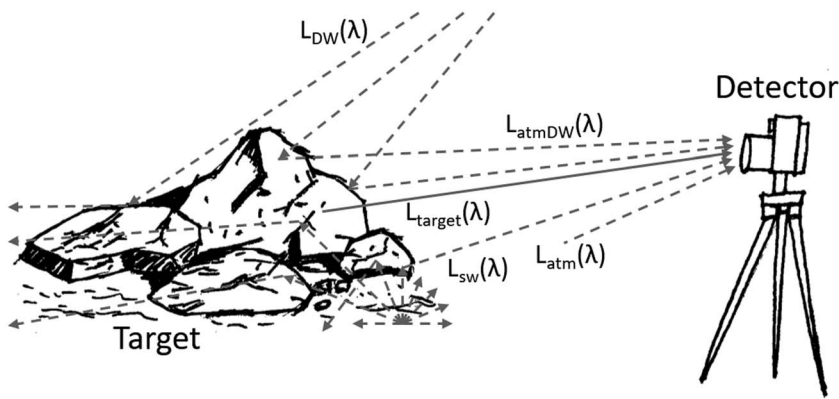


Figure A2. Schematic of radiances measured by the instrument. The distance between the detector and the target is close enough in most cases that $L_{atm}(\lambda)$ is small. Unless the target is a steeply sloping rock face close to near-isotropically scattering surfaces, $L_{sw}(\lambda)$ contribution is also small.

$$B(\lambda, T) = \frac{2hc^2}{\lambda^5} \frac{1}{e^{(hc/\lambda k_B)} - 1}, \quad (\text{A2})$$

where T is temperature, h is the Planck constant (6.626×10^{-34} J/s), c is the speed of light in vacuum (3.0×10^8 m/s), and k_B is the Boltzmann constant (1.381×10^{-23} J/K). $L_{atmDW}(\lambda) = R(\lambda)L_{DW}(\lambda)$ is dependent on surface reflectance ($R(\lambda)$) and the downwelling radiance ($L_{DW}(\lambda)$). For our work, the detector is sufficiently close to the targets in the scene that we can assume that $L_{atm}(\lambda)$ is small (Horton et al., 1998). $L_{sw}(\lambda)$ is a significant factor when the target is a steeply sloping rock face with warmer, near-isotropically scattering surfaces (e.g., soil and ash) in close proximity (further discussed in section 5). In other cases, only minor proportions of sidewelling radiances will be scattered toward the detector, making $L_{sw}(\lambda)$ contribution small. With these assumptions, equation (A1) can be written as

$$L_{meas}(\lambda) = \varepsilon(\lambda)B(T, \lambda) + R(\lambda)L_{DW}(\lambda). \quad (\text{A3})$$

Emissivity and reflectance are related according to Kirchoff's law, $R(\lambda) + \tau(\lambda) + \varepsilon(\lambda) = 1$, where transmissivity, $\tau(\lambda)$, is 0 for optically thick materials, making $R(\lambda) + \varepsilon(\lambda) = 1$ (Hapke, 1993; Salisbury, 1993). Rewriting the above equation leads to

$$\varepsilon(\lambda) = \frac{L_{meas}(\lambda) - L_{DW}(\lambda)}{B(T, \lambda) - L_{DW}(\lambda)} \quad (\text{A4})$$

(Hook & Kahle, 1996; Horton et al., 1998; Kirkland et al., 2002; Korb et al., 1996).

To retrieve $L_{meas}(\lambda)$, raw instrument data number ($DN(\lambda)$) must be converted to radiance by determining the instrument response function, $F_{resp}(\lambda)$, and instrument radiance, $O(\lambda)$. This is done using

$$L_{meas}(\lambda) = \frac{DN_{meas}(\lambda) - O(\lambda)}{F_{resp}(\lambda)} \quad (\text{A5})$$

where $DN_{meas}(\lambda)$ is the raw detector data number as a function of wavelength. $F_{resp}(\lambda)$ can be determined from two blackbody targets at different temperatures (T_1 and T_2 ; Ruff et al., 1997):

$$F_{resp}(\lambda) = \frac{DN_1(\lambda) - DN_2(\lambda)}{B(T_1, \lambda) - B(T_2, \lambda)}. \quad (\text{A6})$$

$O(\lambda)$ is computed as

$$O(\lambda) = DN_{meas}(\lambda) - (F_{resp}(\lambda) \times B(T_1, \lambda)). \quad (\text{A7})$$

The specific configuration of blackbody targets in this study is described in section A3.

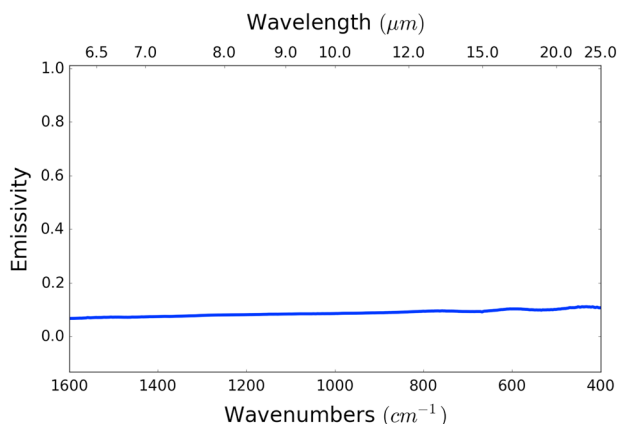


Figure A3. Emissivity of diffuse aluminum foil measured in laboratory.

The downwelling radiance, $L_{DW}(\lambda)$, describes the atmospheric radiance reflected by the target to the sensor. The downwelling radiance primarily affects the emissivity spectral contrast while maintaining spectral shape. In our work, spectral variabilities are detected and presented in relative terms, that is, spectral shape, which is not heavily based on absolute emissivity. Additionally, correcting for downwelling radiance necessitates calibration targets to be placed in the scenes, which may not be always possible in geological field work. For these reasons, we do not correct for downwelling radiance with the exception of Scenes 2 and 4. The downwelling radiance can be measured with a conventional reflectance standard, such as gold or aluminum plate. We measure downwelling radiance using diffuse aluminum foil, which has close to uniform reflectance, and, hence, emissivity, (Figure A3) within the thermal infrared wavelengths, placed in the scene (Figure A4a). $L_{DW}(\lambda)$, then, can be written as

$$L_{DW}(\lambda) = \frac{L_{Al}(\lambda) - \varepsilon_{Al}(\lambda)B(T_{Al}, \lambda)}{1 - \varepsilon_{Al}(\lambda)} \quad (A8)$$

where subscript Al indicates aluminum.

The Planck blackbody function of the targets, $B(\lambda, T)$, in equation (A4) is usually not known. To estimate $B(\lambda, T)$, we utilized the emissivity normalization method (Realmuto, 1990). First, the brightness temperature at each wavelength was computed from equations (A2) and (A3) by assuming a constant emissivity of 1.0. We then found the maximum brightness temperature among all wavelengths and use this as the kinetic temperature. This kinetic temperature was then used to compute $B(\lambda, T)$.

A3. Planck Blackbody Function and Blackbody Calibration Targets

The computation of instrument response function, $F_{resp}(\lambda)$, in equation (A6) relies on two sets of raw detector data number, $DN_{meas}(\lambda)$, and Planck blackbody function, $B(\lambda, T)$, for targets with known blackbody properties (i.e., temperature and emissivity). The *blackbody* targets (Figure A4a) are constructed of aluminum squares with dimensions $20.32 \times 20.32 \times 1.27$ cm and have deep v-shaped parallel grooves (Figure A4b) that exhibit near-unity spectral emissivity across our measured wavelength range due to a *cavity blackbody effect*. These targets were designed with groove depth and spacing following the Mars Exploration Rover Miniature

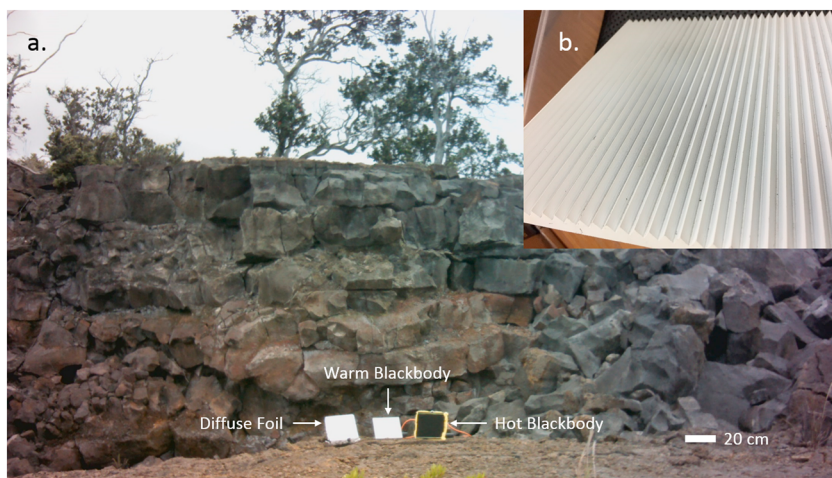


Figure A4. (a) Calibration setup. There are three calibration targets where two are blackbody targets. (b) A closer image of a blackbody target. Grooves create blackbody cavities with approximately unity emissivity across the wavelength range. *Hot blackbody* is heated in order to get the necessary temperature difference. *Diffuse foil* is a crumpled sheet of kitchen aluminum foil secured to a box; spectral measurements of the diffuse foil reflect downwelling radiance from the sky, providing a means to estimate this contribution.

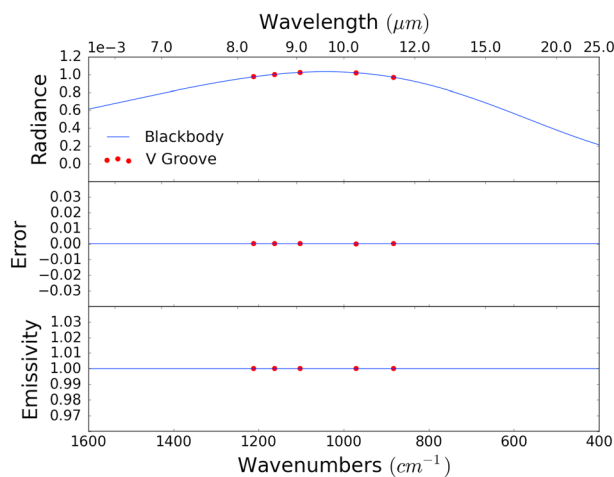


Figure A5. (top) Radiance, in $\text{W} \cdot \text{cm}^{-2} \cdot \text{sr}^{-1} \cdot \mu\text{m}^{-1}$, emitted by the v-groove calibration target (black) at 29 °C and an ideal blackbody computed using equation (A2) for 29 °C. (middle) The error (difference) between the v-groove calibration target and blackbody radiances. (bottom) Emissivity of the v-groove calibration target and blackbody. Radiance measurements of the v-groove calibration target were made with the multispectral frame imager placed within half a meter of the target with negligible downwelling radiance in a laboratory setting. Conversion of digital numbers to radiance and emissivity is based on equations (A5)–(A7) where 21.4 °C and 40.0 °C were used for T_1 and T_2 , respectively.

also placed in the scene to characterize downwelling atmospheric radiance; this would be unnecessary for airless bodies and would likely be only a minor contributor to spectral radiance on Mars. In summary, external calibration targets might be required depending on the instrument design and/or planetary body, but they are not required to be placed within scenes and thus should not be considered a limitation of infrared imaging in a crewed or robotic mission.

A4. Target Temperature Uncertainty

We assume that the temperature of the targets within the scenes does not change considerably during the time frame of data acquisition. Three to 5 min are typically required for collecting data, which is short compared to the time scale needed to naturally change target temperatures significantly in sunny conditions. This assumption may be violated when target body temperatures fluctuate substantially during the time frame of data acquisition, which may occur in partly cloudy conditions. Scattered clouds cast sudden shadows that disrupt the near-steady temperature of target bodies achievable in continuously sunny conditions and rapidly change the temperature.

A5. Artifact Correction for Multispectral Frame Imager

The use of filters in combination with the standard, commercially available thermal imaging camera introduces unwanted optical artifacts to images. The artifacts are manifested as a radial decrease in radiance throughput to the detector (Figure A6) and likely arise from slight differences in radial distance between the filter, which is flat, and lens, which is curved.

We correct these artifacts on raw detector data number ($DN_{\text{meas}}(\lambda)$) images, prior to any subsequent calibration steps, using a *flatfield* correction. Images of a uniform, featureless surface, at constant temperatures, were taken with each of the five filters to characterize the spatial distribution of the radiance throughput across the detector array (Figure A6). To apply the correction, first, the raw detector data number of flatfield images was normalized with the maximum value within each of the flatfield images as

$$DN_{\text{ff, norm}}(\lambda) = \frac{DN_{\text{ff}}(\lambda)}{\max(DN_{\text{ff}}(\lambda))}. \quad (\text{A9})$$

Thermal Emission Spectrometer (Mini-TES) external calibration target (Christensen et al., 2003), and a similar target was also used for Moderate Resolution Imaging Spectroradiometer on Terra and Aqua space crafts of the Earth Observing System (Xiong et al., 2003). We verified the near-unity emissivity of the v-groove calibration targets in the laboratory (Figure A5). One of the blackbody targets is painted black and actively heated, and the other is painted white and not heated; this was done in an effort to maximize the temperature difference between the two. In most cases, at least 15 min of heating was necessary to reach a stable temperature. Temperatures of the targets are recorded during the image acquisition process using attached thermistors. The blackbody targets are placed within the scene of interest, so that external radiance contributions in the optical path (the filters and negligible atmospheric emissions between detector and target) can be accounted for in instrument response function, $F_{\text{resp}}(\lambda)$.

The need for scene calibration targets for the multispectral imager arises solely from the instrument design—the camera cannot rotate easily to view an external calibration target outside of the scene. However, in a planetary mission, the instrument could be designed to rotate and view an external calibration target mounted on the rover (e.g., as the Mars Exploration Rover Pancam and Mini-TES instruments did). Furthermore, depending on the instrument design (such as whether there is an immovable lens or window in the optical path between the scene and detector), even an externally mounted target might not be required. Foil panels were

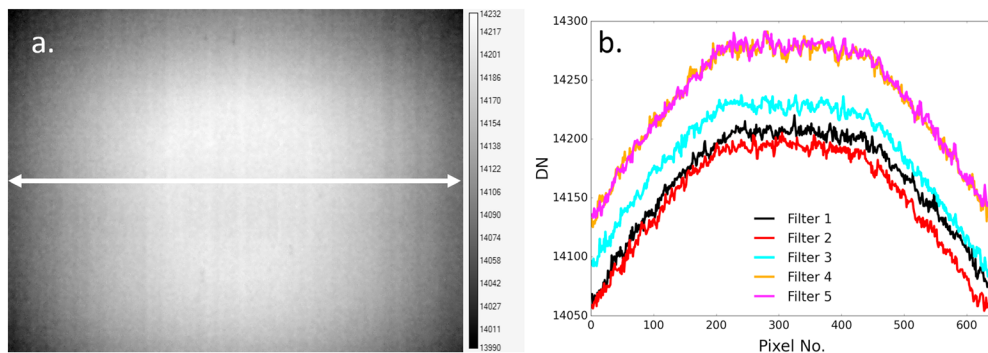


Figure A6. (a) Radial decrease in radiance seen in filter 1 ($8.3 \mu\text{m}$, $1,211.8 \text{ cm}^{-1}$). Filters 2–5 are not shown but are similar to the pattern observed in filter 1. (b) Profile of instrument DN across the middle of the image in each of the filters (indicated with arrow in (a)).

where $DN_{\text{ff, norm}}(\lambda)$ and $DN_{\text{ff}}(\lambda)$ are raw detector data numbers for normalized flatfield and original flatfield images, respectively. Then, flatfield-corrected raw detector data numbers, $DN_{\text{fmeas, ff}}(\lambda)$, were computed as

$$DN_{\text{meas, ff}}(\lambda) = DN_{\text{ff}}(\lambda) \times (1 + (1 - DN_{\text{ff, norm}})). \quad (\text{A10})$$

Several flatfield images were acquired for surfaces and filters at different temperatures in order to see if temperature has a significant contribution to the spatial distribution or magnitude of the radiance throughput. We found that changing filter and surface temperatures had minor effects on these artifacts; thus, temperature effect can be neglected in room and typical daytime temperatures of our field sites.

We did not perform pixel-by-pixel correction for sensor nonuniformities.

Acknowledgments

Field work was assisted by Michael. T. Thorpe, Marcella H. Yant, Nicholas D. DiFrancesco, Erin Fitch, and Alexandra Ahern. Laboratory spectral measurements were assisted by Kristina M. Finnelli. This work was supported by the RIS⁴E node of NASA's Solar System Exploration Virtual Institute (SSERVI) (T. D. G., PI). Data presented in this work will be placed on the Stony Brook Academic Commons permanent archive (<http://commons.library.stonybrook.edu/>).

References

- Abbot, E. A., Gillespie, A. R., & Kahle, A. B. (2013). Thermal infrared imaging of weathering and alteration changes on the surfaces of basalt flows, Hawai'i, USA. *International Journal of Remote Sensing*, 34(9–10), 3332–3355. <https://doi.org/10.1080/01431161.2012.716920>
- Abercromby, A. F. J., Gernhardt, M. L., & Jadwick, J. (2013). Evaluation of dual multi-mission space exploration vehicle operations during simulated planetary surface exploration. *Acta Astronautica*, 90(2), 203–214. <https://doi.org/10.1016/j.actaastro.2012.02.022>
- Abrams, M., Abbott, E., & Kahle, A. (1991). Combined use of visible, reflected infrared, and thermal infrared images for mapping Hawaiian lava flows. *Journal of Geophysical Research*, 96(B1), 475–484. <https://doi.org/10.1029/90JB01392>
- Almeida, R. M. (1992). Detection of LO modes in glass by infrared reflection spectroscopy at oblique incidence. *Physical Review B*, 45(1), 161–170. <https://doi.org/10.1103/PhysRevB.45.161>
- Anthony, E. Y., Hoffer, J. M., Waggoner, W. K., & Chen, W. (1992). Compositional diversity in late Cenozoic mafic lavas in the Rio Grande rift and Basin and Range province, southern New Mexico. *Geological Society of America Bulletin*, 104(8), 973–979. [https://doi.org/10.1130/0016-7606\(1992\)104<0973:CDILCM>2.3.CO;2](https://doi.org/10.1130/0016-7606(1992)104<0973:CDILCM>2.3.CO;2)
- Chemtob, S. M., Jolliff, B. L., Rossman, G. R., Eiler, J. M., & Arvidson, R. E. (2010). Silica coatings in the Ka'u Desert, Hawaii, a Mars analog terrain: A micromorphological, spectral, chemical, and isotopic study. *Journal of Geophysical Research*, 115, E04001. <https://doi.org/10.1029/2009JE003473>
- Christensen, P. R., Bandfield, J. L., Hamilton, V. E., Howard, D. A., Lane, M. D., Piatek, J. L., et al. (2000). A thermal emission spectral library of rock-forming minerals. *Journal of Geophysical Research*, 105(E4), 9735–9739. <https://doi.org/10.1029/1998JE000624>
- Christensen, P. R., Bandfield, J. L., Hamilton, V. E., Ruff, S. W., Kieffer, H. H., Titus, T. N., et al. (2001). Mars Global Surveyor Thermal Emission Spectrometer experiment: Investigation description and surface science results. *Journal of Geophysical Research*, 106(E10), 23,823–23,871. <https://doi.org/10.1029/2000JE001370>
- Christensen, P. R., & Harrison, S. T. (1993). Thermal infrared emission spectroscopy of natural surfaces: Application to desert varnish coatings on rocks. *Journal of Geophysical Research*, 98(B11), 19,819–19,834. <https://doi.org/10.1029/93JB00135>
- Christensen, P. R., Mehall, G. L., Silverman, S. H., Anwar, S., Cannon, G., Gorelick, N., et al. (2003). Miniature Thermal Emission Spectrometer for the Mars Exploration Rovers. *Journal of Geophysical Research*, 108(E12), 8064. <https://doi.org/10.1029/2003JE002117>
- Conel, J. E. (1969). Infrared emissivities of silicates: Experimental results and a cloudy atmosphere model of spectral emission from condensed particulate mediums. *Journal of Geophysical Research*, 74(6), 1614–1634. <https://doi.org/10.1029/JB074i006p01614>
- Cooper, F. J., Adams, B. A., Edwards, C. S., & Hodges, K. V. (2012). Large normal-sense displacement on the South Tibetan fault system in the eastern Himalaya. *Geology*, 40(11), 971–974. <https://doi.org/10.1130/g33318.1>
- Crisp, J., Kahle, A. B., & Abbott, E. A. (1990). Thermal infrared spectral character of Hawaiian basaltic glasses. *Journal of Geophysical Research*, 95(B13), 21,657–21,669. <https://doi.org/10.1029/JB095iB13p21657>
- Darton, N. H. (1916). Explosion craters. *Scientific Monthly*, 2, 417–430.
- Easton, R. M. (1987). Stratigraphy of Kilauea Volcano. In R. W. Decker, T. L. Wright, & P. H. Stauffer (Eds.), *Volcanism in Hawaii*, U.S. Geological Survey Professional Paper (Vol. 1350, pp. 243–260). Washington, DC: United States Government Printing Office.

- Eppler, D., Adams, B., Archer, D., Baiden, G., Brown, A., Carey, W., et al. (2013). Desert Research and Technology Studies (DRATS) 2010 science operations: Operational approaches and lessons learned for managing science during human planetary surface missions. *Acta Astronautica*, 90(2), 224–241. <https://doi.org/10.1016/j.actaastro.2012.03.009>
- Farmer, V. C. (1974). The Infrared Spectra of Minerals (Vol. 4, 539 pp.). *Mineralogical Society of Great Britain and Ireland*. London. <https://doi.org/10.1180/mono-4>
- Feely, K. C., & Christensen, P. R. (1999). Quantitative compositional analysis using thermal emission spectroscopy: Application to igneous and metamorphic rocks. *Journal of Geophysical Research*, 104(E10), 24,195–24,210. <https://doi.org/10.1029/1999JE001034>
- Gabrieli, A., Wright, R., Lucey, P. G., Porter, J. N., Garbeil, H., Pilger, E., & et al. (2016). Characterization and initial field test of an 8–14 μm thermal infrared hyperspectral imager for measuring SO_2 in volcanic plumes. *Bulletin of Volcanology*, 78(10), 73.
- Gillespie, A. R., Kahle, A. B., & Walker, R. F. (1986). Color enhancement of highly correlated images: I. Decorrelation and HIS contrast stretches. *Remote Sensing of Environment*, 20(3), 209–235. [https://doi.org/10.1016/0034-4257\(86\)90044-1](https://doi.org/10.1016/0034-4257(86)90044-1)
- Glotch, T. D., Dyer, M. D., Bleacher, J. E., Schoonen, M. A. A., Petro, N. E., Jones, A. J. P., & The RIS⁴E Team (2015). Remote, In-Situ and Synchrotron Studies for Science and Exploration (RIS⁴E): First year of science and exploration, Paper presented at Lunar and Planetary Science Conference 46, Abstract2178.
- Greenberger, R. N., Mustard, J. F., Cloutis, E. A., Mann, P., Wilson, J. H., Flemming, R. L., et al. (2015). Hydrothermal alteration and diagenesis of terrestrial lacustrine pillow basalts: Coordination of hyperspectral imaging with laboratory measurements. *Geochimica et Cosmochimica Acta*, 171, 174–200. <https://doi.org/10.1016/j.gca.2015.08.024>
- Greenberger, R. N., Mustard, J. F., Cloutis, E. A., Pratt, L. M., Sauer, R. E., Mann, P., et al. (2015). Serpentinitization, iron oxidation, and aqueous conditions in an ophiolite: Implications for hydrogen production and habitability on Mars. *Earth and Planetary Science Letters*, 416, 21–34. <https://doi.org/10.1016/j.epsl.2015.02.002>
- Greenberger, R. N., Mustard, J. F., Ehlmann, B. L., Blaney, D. L., Cloutis, E. A., Wilson, J. H., et al. (2015). Imaging spectroscopy of geological samples and outcrops: Novel insights from microns to meters. *GSA Today*, 25(12), 4–10. <https://doi.org/10.1130/GSATG252A.1>
- Hamilton, V. E., & Christensen, P. R. (2000). Determining the modal mineralogy of mafic and ultramafic igneous rocks using thermal infrared emission spectroscopy. *Journal of Geophysical Research*, 105(E4), 9717–9733. <https://doi.org/10.1029/1999JE001113>
- Hamilton, V. E., Wyatt, M. B., McSween, H. Y. Jr., & Christensen, P. R. (2001). Analysis of terrestrial and Martian volcanic compositions using thermal emission spectroscopy: 2. Application to Martian surface spectra from the Mars Global Surveyor Thermal Emission Spectrometer. *Journal of Geophysical Research*, 106(E7), 14,733–14,746. <https://doi.org/10.1029/2000JE001353>
- Hapke, B. (1993). *Theory of reflectance and emittance spectroscopy*. New York, NY: Cambridge University Press. <https://doi.org/10.1017/CBO9780511524998>
- Holcomb, R. T. (1987). Eruptive history and long-term behavior of Kilauea Volcano. In R. W. Decker, T. L. Wright, & P. H. Stauffer (Eds.), *Volcanism in Hawaii*, U.S. Geological Survey Professional Paper (Vol. 1350, pp. 261–350). Washington, DC: United States Government Printing Office.
- Hook, S. J., & Kahle, A. B. (1996). The micro Fourier transform interferometer (μFTIR)—A new field spectrometer for acquisition of infrared data of natural surfaces. *Remote Sensing of Environment*, 56(3), 172–181. [https://doi.org/10.1016/0034-4257\(95\)00231-6](https://doi.org/10.1016/0034-4257(95)00231-6)
- Horton, K. A., Johnson, J. R., & Lucey, P. G. (1998). Infrared measurements of pristine and disturbed soils: 2. Environmental effects and field data reduction. *Remote Sensing of Environment*, 64(1), 47–52. [https://doi.org/10.1016/S0034-4257\(97\)00167-3](https://doi.org/10.1016/S0034-4257(97)00167-3)
- Hörz, F., Lofgren, G. E., Gruener, J. E., Eppler, D. B., Skinner Jr., J. A., Fortezzo, C. M., et al. (2013). The traverse planning process for D-RATS 2010. *Acta Astronautica*, 90, 254–267. <https://doi.org/10.1016/j.actaastro.2012.02.008>
- Hunt, G. R., & Vincent, R. K. (1968). The behavior of spectral features in the infrared emission from particulate surfaces of various grain sizes. *Journal of Geophysical Research*, 73(18), 6039–6046. <https://doi.org/10.1029/JB073i018p06039>
- Hurtado, J. M. Jr., Young, K., Bleacher, J. E., Garry, W. B., & Rice, J. W. Jr. (2013). Field geologic observation and sample collection strategies for planetary surface exploration: Insights from the 2010 Desert RATS geologist crewmembers. *Acta Astronautica*, 90(2), 344–355. <https://doi.org/10.1016/j.actaastro.2011.10.015>
- Ito, G., Arnold, J. A., & Glotch, T. D. (2017). T-matrix and radiative transfer hybrid models for densely packed particulates at mid-infrared wavelengths. *Journal of Geophysical Research: Planets*, 122, 822–838. <https://doi.org/10.1002/2017JE005271>
- Ito, G., Mishchenko, M. I., & Glotch, T. D. (2018). Radiative-transfer modeling of spectra of planetary regoliths using cluster-based dense packing modifications. *Journal of Geophysical Research: Planets*, 123, 1203–1220. <https://doi.org/10.1029/2018JE005532>
- Kahle, A. B., Gillespie, A. R., Abbott, E. A., Abrams, M. J., Walker, R. E., Hoover, G., & et al. (1988). Relative dating of Hawaiian lava flows using multispectral thermal infrared images: A new tool for geologic mapping of young volcanic terranes. *Journal of Geophysical Research*, 93(B12), 15,239–15,251. <https://doi.org/10.1029/JB093iB12p15239>
- Kahle, A. B., & Goetz, A. F. H. (1983). Mineralogical information from a new airborne thermal infrared multispectral scanner. *Science*, 222(4619), 24–27. <https://doi.org/10.1126/science.222.4619.24>
- Kahle, A. B., Palluconi, F. D., & Christensen, P. R. (1993). Thermal emission spectroscopy: Application to the Earth and Mars. In C. Pieters, & P. Englert (Eds.), *Remote geochemical analysis: Elemental and mineralogical composition* (pp. 99–120). New York, NY: Cambridge University Press.
- Kirkland, L., Herr, K., Keim, E., Adams, P., Salisbury, J., Hackwell, J., & et al. (2002). First use of an airborne thermal infrared hyperspectral scanner for compositional mapping. *Remote Sensing of Environment*, 80(3), 447–459. [https://doi.org/10.1016/S0034-4252\(01\)00323-6](https://doi.org/10.1016/S0034-4252(01)00323-6)
- Korb, A. R., Dybwad, P., Wadsworth, W., & Salisbury, J. W. (1996). Portable Fourier transform infrared spectroradiometer for field measurements of radiance and emissivity. *Applied Optics*, 35(10), 1679–1692. <https://doi.org/10.1364/AO.35.001679>
- Lane, M. D., & Christensen, P. R. (1997). Thermal infrared emission spectroscopy of anhydrous carbonates. *Journal of Geophysical Research*, 102(E11), 25,581–25,592. <https://doi.org/10.1029/97JE02046>
- Lane, M. D., & Christensen, P. R. (1998). Thermal infrared emission spectroscopy of salt minerals predicted for Mars. *Icarus*, 135, 528–536.
- Lawson, C. L., & Hanson, R. J. (1974). *Solving least-squares problems*. Englewood Cliffs, NJ: Prentice-Hall.
- Lyon, R. J. P. (1963). Evaluation of infrared spectrophotometry for compositional analysis of lunar and planetary soils. In *Stanford Research Institute Final Report under Contract NASr* (118 pp.). Menlo Park, CA: Stanford Research Institute.
- Malin, M. C., Dzurisin, D., & Sharp, R. P. (1983). Stripping of Keanakakoi tephra on Kilauea Volcano, Hawaii. *Bulletin of the Geological Society of America*, 94(10), 1148–1158. [https://doi.org/10.1130/0016-7606\(1983\)94<1148:SOKTOK>2.0.CO;2](https://doi.org/10.1130/0016-7606(1983)94<1148:SOKTOK>2.0.CO;2)
- Minniti, M. E., Weitz, C. M., Lane, M. D., & Bishop, J. L. (2007). Morphology, chemistry, and spectral properties of Hawaiian rock coatings and implications for Mars. *Journal of Geophysical Research*, 112, E05015. <https://doi.org/10.1029/2006JE002839>
- Mishchenko, M. I. (2009). Electromagnetic scattering by nonspherical particles: A tutorial review. *Journal of Quantitative Spectroscopy and Radiative Transfer*, 110(11), 808–832. <https://doi.org/10.1016/j.jqsrt.2008.12.005>

- Mishchenko, M. I. (2014). *Electromagnetic scattering by particles and particle groups: An introduction*. Cambridge, UK: Cambridge University Press. <https://doi.org/10.1017/CBO9781139019064>
- Moersch, J. E., & Christensen, P. R. (1995). Thermal emission from particulate surfaces: A comparison of scattering models with measured spectra. *Journal of Geophysical Research*, 100(E4), 7465–7477.
- Mustard, J. F., & Hays, J. E. (1997). Effects of hyperfine particles on reflectance spectra from 0.3 to 25 μm . *Icarus*, 125, 145–163.
- Pitman, K. M., Wolff, M. J., & Clayton, G. C. (2005). Application of modern radiative transfer tools to model laboratory quartz emissivity. *Journal of Geophysical Research*, 110, E08003. <https://doi.org/10.1029/2005JE002428>
- Prata, A. J., & Bernardo, C. (2009). Retrieval of volcanic ash particle size, mass and optical depth from a ground-based thermal infrared camera. *Journal of Volcanology and Geothermal Research*, 186(1–2), 91–107. <https://doi.org/10.1016/j.jvolgeores.2009.02.007>
- Prata, A. J., & Bernardo, C. (2014). Retrieval of sulfur dioxide from a ground-based thermal infrared imaging camera. *Atmospheric Measurement Techniques*, 7(9), 2807–2828. <https://doi.org/10.5194/amt-7-2807-2014>
- Ramsey, M. S., & Christensen, P. R. (1998). Mineral abundance determination: Quantitative deconvolution of thermal emission spectra. *Journal of Geophysical Research*, 103(B1), 577–596. <https://doi.org/10.1029/97JB02784>
- Ramsey, M. S., & Harris, A. J. L. (2012). Volcanology 2020: How will thermal remote sensing of volcanic surface activity evolve over the next decade? *Journal of Volcanology and Geothermal Research*, 249, 217–233.
- Realmuto, V. (1990). Separating the effects of temperature and emissivity: Emissivity spectrum normalization. Paper presented at proceedings of the second TIMS workshop. *Jet Propulsion Laboratory Publication*, 90-55, 26–30.
- Rogers, A. D., & Aharonson, O. (2008). Mineralogical composition of sands in Meridiani Planum determined from Mars Exploration Rover data and comparison to orbital measurements. *Journal of Geophysical Research*, 113, E06S14. <https://doi.org/10.1029/2007JE002995>
- Ross, A., Kosmo, J., & Janoiko, B. (2013). Historical synopses of desert RATS 1997–2010 and a preview of desert RATS 2011. *Acta Astronautica*, 90(2), 182–202. <https://doi.org/10.1016/j.actaastro.2012.02.003>
- Rowan, L. C., Hook, S. J., Abrams, M. J., & Mars, J. C. (2003). Mapping hydrothermally altered rocks at Cuprite, Nevada, using the Advanced Spaceborne Thermal Emission and Reflection Radiometer (ASTER): A new satellite-imaging system. *Economic Geology*, 98(5), 1019–1027. <https://doi.org/10.2113/gsecongeo.98.5.1019>
- Rowan, L. C., Mars, J. C., & Simpson, C. J. (2005). Lithologic mapping of the Mordor, NT, Australia ultramafic complex by using the Advanced Spaceborne Thermal Emission and Reflection Radiometer (ASTER). *Remote Sensing of Environment*, 99(1–2), 105–126. <https://doi.org/10.1016/j.rse.2004.11.021>
- Ruff, S. W., Farmer, J. D., Calvin, W. M., Herkenhoff, K. E., Johnson, J. R., Morris, R. V., et al. (2011). Characteristics, distribution, origin, and significance of opaline silica observed by the Spirit rover in Gusev crater, Mars. *Journal of Geophysical Research*, 116, E00F23. <https://doi.org/10.1029/2010JE003767>
- Ruff, W. R., Christensen, P. R., Parbera, P. W., & Anderson, D. L. (1997). Quantitative thermal emission spectroscopy of minerals: A laboratory technique for measurement and calibration. *Journal of Geophysical Research*, 102(B7), 14,899–14,913. <https://doi.org/10.1029/97JB00593>
- Sabine, C. (1999). Remote sensing strategies for mineral exploration. In A. N. Rencz (Ed.), *Remote sensing for the Earth sciences: Manual of remote sensing*, (3rd ed., Vol. 3, pp. 375–447). New York, NY: John Wiley.
- Salisbury, J. W. (1993). Mid-infrared spectroscopy: Laboratory data. In C. Pieters, & P. Englert (Eds.), *Remote geochemical analysis: Elemental and mineralogical composition*, (pp. 79–98). New York, NY: Cambridge Univ. Press.
- Salisbury, J. W., & Walter, L. S. (1989). Thermal infrared (2.5–13.5 μm) spectroscopic remote sensing of igneous rock types on particulate planetary surfaces. *Journal of Geophysical Research*, 94(B7), 9192–9202. <https://doi.org/10.1029/JB094iB07p09192>
- Salisbury, J. W., Walter, L. S., Vergo, N., & D'Aria, D. M. (1991). *Infrared (2.1–25 μm) spectra of minerals*. Baltimore, MD: Johns Hopkins Univ. Press.
- Schiffman, P., Zierenberg, R., Marks, N., Bishop, J. L., & Dyar, M. D. (2006). Acid-fog deposition at Kilauea volcano: A possible mechanism for the formation of siliceous-sulfate rock coatings on Mars. *Geology*, 34(11), 921–924. <https://doi.org/10.1130/G22620A.1>
- Seager, W. R. (1987). Caldera-like collapse of Kilbourne Hole maar, New Mexico. *New Mexico Geology*, 9, 69–73.
- Seelos, K. D., Arvidson, R. E., Jolliff, B. L., Chemtob, S. M., Morris, R. V., Ming, D. W., et al. (2010). Silica in a Mars analog environment: Ka'u Desert, Kilauea Volcano, Hawaii. *Journal of Geophysical Research*, 115, E00D15. <https://doi.org/10.1029/2009JE003347>
- Sperazza, M., Moore, J. N., & Hendrix, M. S. (2004). High-resolution particle size analysis of naturally occurring very fine-grained sediment through laser diffractometry. *Journal of Sedimentary Research*, 74(5), 736–743. <https://doi.org/10.1306/031104740736>
- Squyres, S. W., Arvidson, R. E., Ruff, S., Gellert, R., Morris, R. V., Ming, D. W., et al. (2008). Detection of silica-rich deposits on Mars. *Science*, 320(5879), 1063–1067. <https://doi.org/10.1126/science.1155429>
- Thompson, R. N., Ottley, C. J., Smith, P. M., Pearson, D. G., Dickin, A. P., Morrison, M. A., et al. (2005). Source of the Quaternary alkalic basalts, picrites and basanites of the Pothiroli Volcanic Field, New Mexico, USA: Lithosphere or convecting mantle? *Journal of Petrology*, 46(8), 1603–1643. <https://doi.org/10.1093/petrology/egi028>
- Thorpe, M. T., Rogers, A. D., Bristow, T. F., & Pan, C. (2015). Quantitative compositional analysis of sedimentary materials using thermal emission spectroscopy: 1. Application to sedimentary rocks. *Journal of Geophysical Research: Planets*, 120, 1956–1983. <https://doi.org/10.1002/2015JE004863>
- Tirsch, D., Craddock, R. A., Platz, T., Maturilli, A., Helbert, J., & Jaumann, R. (2012). Spectral and petrologic analyses of basaltic sands in Ka'u Desert (Hawaii)—Implications for the dark dunes on Mars. *Earth Surface Processes and Landforms*, 37(4), 434–448. <https://doi.org/10.1002/esp.2266>
- Van de Hulst, H. C. (1957). *Light scattering by small particles*. New York, NY: John Wiley.
- Vincent, R. K., & Thomson, F. (1972). Spectral compositional imaging of silicate rocks. *Journal of Geophysical Research*, 77(14), 2465–2472. <https://doi.org/10.1029/JB077i014p02465>
- Walter, L. S., & Salisbury, J. W. (1989). Spectral characterization of igneous rocks in the 8- to 12- μm region. *Journal of Geophysical Research*, 94(B7), 9203–9213. <https://doi.org/10.1029/JB094iB07p09203>
- Wilson, E. B. Jr., Decius, J. C., & Cross, P. C. (1955). *Molecular vibrations: The theory of infrared and Raman vibrational spectra* (388 pp.). McGraw-Hill, New York.
- Wright, R., Lucey, P., Crites, S., Horton, K., Wood, M., & Garbeil, H. (2013). BBM/EM design of the thermal hyperspectral imager: An instrument for remote sensing of earth's surface, atmosphere and ocean, from a microsatellite platform. *Acta Astronautica*, 87, 182–192. <https://doi.org/10.1016/j.actaastro.2013.01.001>
- Wright, T. L. (1971). *Chemistry of Kilauea and Mauna Loa in space and time*, U.S. Geological Survey Professional Paper, (Vol. 735). Washington, DC: United States Government Printing Office.
- Wyatt, M. B., Hamilton, V. E., McSween, H. Y. Jr., Christensen, P. R., & Taylor, L. A. (2001). Analysis of terrestrial and Martian volcanic compositions using thermal emission spectroscopy: 1. Determination of mineralogy, chemistry, and classification strategies. *Journal of Geophysical Research*, 106(E7), 14,711–14,732. <https://doi.org/10.1029/2000JE001356>

- Xiong, X., Chiang, K., Esposito, J., Guenther, B., & Barnes, W. (2003). MODIS on-orbit calibration and characterization. *Metrologia*, 40(1), S89–S92. <https://doi.org/10.1088/0026-1394/40/1/320>
- Young, K., Hurtado, J. M. Jr., Bleacher, J. E., Garry, W. B., Bleisath, S., Buffington, J., & et al. (2013). Tools and technologies needed for conducting planetary field geology while on EVA: Insights from the 2010 Desert RATS geologist crewmembers. *Acta Astronautica*, 90(2), 332–343. <https://doi.org/10.1016/j.actaastro.2011.10.016>
- Young, K. E., Bleacher, J. E., Rogers, A. D., Schmitt, H. H., McAdam, A. C., Gary, W. B., et al. (2018). The incorporation of field portable instrumentation into human planetary surface exploration. *Earth and Space Science*, 5. <https://doi.org/10.1029/2018EA000378>, in press
- Young, K. E., Evans, C. A., Hodges, K. V., Bleacher, J. E., & Graff, T. G. (2016). A review of the handheld X-ray fluorescence spectrometer as a tool for field geologic investigations on Earth and in planetary surface exploration. *Applied Geochemistry*, 72, 77–87. <https://doi.org/10.1016/j.apgeochem.2016.07.003>